Mechanism and Machine Theory 143 (2020) 103614

Contents lists available at ScienceDirect

Mechanism and Machine Theory

journal homepage: www.elsevier.com/locate/mechmachtheory

Research paper

Time efficient stiffness model computation for a parallel haptic mechanism via the virtual joint method

İbrahimcan Görgülü [a,*], Giuseppe Carbone [b,c], Mehmet İsmet Can Dede [a]

[a] Izmir Institute of Technology, Turkey
[b] DIMEG University of Calabria, Italy
[c] TU Cluj-Napoca, Romania

ARTICLE INFO

Article history:
Received 30 July 2019
Revised 26 August 2019
Accepted 8 September 2019
Available online 26 September 2019

Keywords:
Stiffness
Parallel manipulator
Virtual joint method
Haptic mechanism

ABSTRACT

Haptic devices are used for displaying a range of mechanical impedance values to the user. This impedance is regulated by a real-time control loop depending on the position information of the end-effector, which is usually acquired indirectly by using forward kinematics equations. Nevertheless, the kinematic model is insufficient to obtain accurate values if there are non-negligible compliant displacements. This gives a strong motivation for implementing a real-time stiffness model in the haptic control loop for improving its accuracy. Additionally, stiffness performance indices can be used at the design stage for enhancing the haptic devices impedance range within optimal design procedures. Fast solutions of a stiffness model are required for a real-time control as well as for decreasing the optimization time during a design process with a trade-off between accuracy and computational costs. In this study, we propose a computation time-efficient stiffness analysis of a parallel haptic device mechanism. The accuracy and computational costs of the proposed model are calculated and compared with a model that is obtained via a finite element method to demonstrate the effectiveness of the proposed approach with the desired real-time and accuracy performance.

1. Introduction

Haptic devices display haptic stimuli to a user [1]. Kinesthetic type haptic devices generate force/torque that is regulated by motion information in order to generate the required impedance output. These devices are used as a master controller to manipulate a slave robot. The essence of haptic feedback is to enhance the telepresence sensation, which is the sense of being present in the remote environment (RE). The realism of telepresence depends on transmission quality of haptic information from the RE to the user via the haptic device. The physical capabilities (PC) of the haptic device determine the transmission quality of haptic information and the performance of the haptic device.

Haptic devices use parallel, serial, or hybrid mechanisms [2–4]. Therefore, the PC of a haptic device depends on the manipulator's mechanical performance. The PC of the manipulator can be increased via an optimal design [5–7]. The design optimization, on the other hand, requires the usage of many performance metrics related to robotics [8,9]. These metrics are computed based on the manipulator's models such as the kinematics, stiffness, and dynamic models. Among these models,

* Corresponding author.
E-mail addresses: ibrahimcangorgulu@iyte.edu.tr (İ. Görgülü), giuseppe.carbone@unical.it (G. Carbone), candede@iyte.edu.tr (M.İ.C. Dede).

https://doi.org/10.1016/j.mechmachtheory.2019.103614
0094-114X/

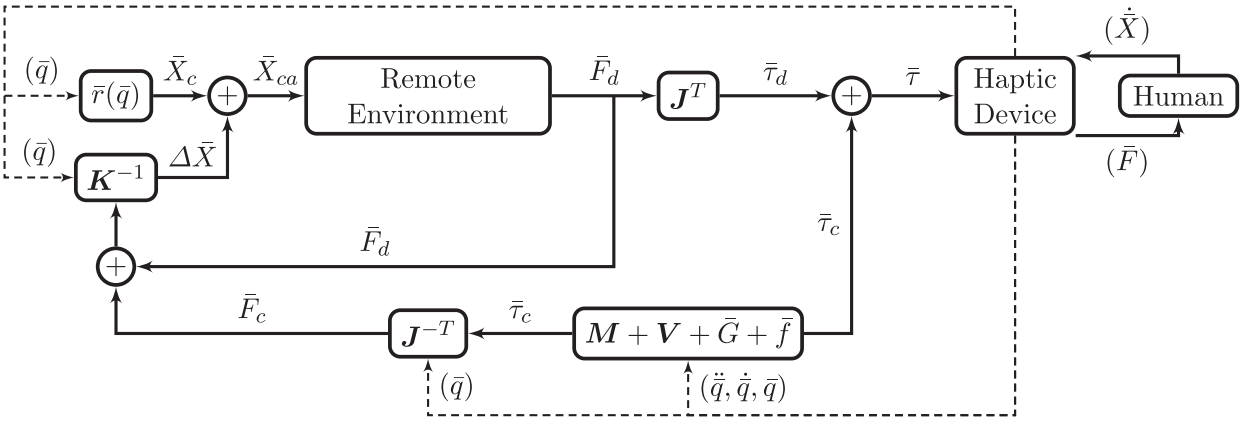

Fig. 1. Haptic control loop; Subscripts *c*, *d*, and *a* indicate the computed, desired, and actual parameters; $\bar{X}$ is the position vector. $\bar{r}(\bar{q})$ denotes the forward kinematics equations to compute the end-effector position by using measured joint positions, $\bar{q}$. $\boldsymbol{J}$ denotes the Jacobian matrix; $\bar{F}$ and $\bar{\tau}$ are the force/torque vectors defined in task and joint space, respectively; $\boldsymbol{M}, \boldsymbol{V}, \bar{G}, \bar{f}$ are the mass, Coriolis-centripetal, gravitation, and friction terms, respectively. The dashed lines denote the measured physical signals via related sensors.

the stiffness model receives special attention in design since high stiffness is needed for enhanced maximum impedance performance [1,10,11]. Hence, an optimal design process requires a stiffness model to be used in the calculation of stiffness performance indices [12–15].

In a general haptic control loop, forward kinematics is used to compute the end effector's motion. This information is used for mapping the motion of the haptic device's end-effector to the motion of the manipulated object in RE. The perception of haptic realism depends on this mapping accuracy. During a haptic interaction, however, the end-effector experiences compliant motions while displaying resistive forces/torques to the user. Hence, a kinematic model alone is not sufficient for achieving accurate mapping. On the other hand, a stiffness model can be used to estimate compliant motions. Then, these estimated compliant motions can be used for compensating the end-effector motion acquisition errors due to the indirect calculation of the end-effector's motion. As a result of this, the motion mapping performance between the master and the slave can be enhanced [16].

The usage of a generic stiffness model, $\boldsymbol{K}$, is shown in Fig. 1 within a haptic control loop. In this loop, all of the measured/calculated forces and torques that are acting on the manipulator are transmitted to the stiffness model to estimate the compliant deflections, $\Delta\bar{X}$. $\Delta\bar{X}$ is combined with the end-effector's position information, which is calculated via forward kinematics, to compute an estimated actual position of the end-effector, $\bar{X}_{ca}$. This estimated position information is used in RE to produce the desired force/torque, $\bar{F}_d$, relatively more accurately.

A control loop needs to operate in real-time. Namely, it should operate with at least 1 kHz sampling frequency to cover all kinesthetic haptic interaction types [1]. Aside from the haptic control loop, design optimization for a haptic device mechanism or any robot manipulator is an iterative process. The speed of the model computations determines the duration of the optimization process. Among the variety of models, generally, stiffness models have a more considerable computation cost. Hence, a computationally efficient stiffness model with acceptable accuracy is required in the design optimization studies.

As in any modeling study, in stiffness modeling, accuracy and computation time are inversely proportional. While slow computations reduce control performance that even may cause control instability due to computation delays, a single design optimization run may extend to several months due to the excessive computation of the stiffness model. Nevertheless, inaccurate but fast computations cannot be used in both scenarios. Compared to serial manipulators, stiffness computations of parallel manipulators consume more time and processor power because they have relatively more links and joints in their closed-loop kinematic structure [17–19]. Hence, both aspects may be addressed by a computationally time-efficient solution of the stiffness model. This study focuses on the derivation of a stiffness model of a parallel manipulator that can run in real-time (less than 1ms computation time) with high accuracy (less than %1 error). A version of R-CUBE parallel mechanism [20] is adopted for stiffness modeling as a case study since it was previously used as a mechanism of a haptic device [21]. The stiffness model of this mechanism is obtained via Virtual Joint Method (VJM). Then, the Finite Element Method (FEM) is used to obtain more accurate results. Later, these results are compared to VJM model's results, in terms of compliant displacements, via their computation time and accuracy. In Section 2, stiffness modeling methods are reviewed, and the reason for selecting VJM is explained. In Section 3, brief information on the kinematics of R-CUBE mechanism and its detailed stiffness model are presented. In Section 4, FEM model of the manipulator that is constructed by using ANSYS Workbench software is provided along with the description of the simulation setup. In Section 5, the results of the model validation procedure and computation time calculations are presented. Finally, in Section 6, the outcomes are discussed.

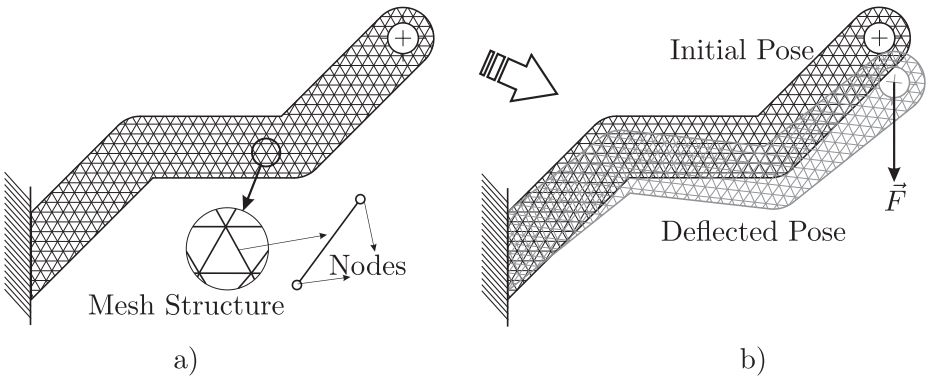

Fig. 2. FEM model of a link: (a) mesh structure and its zoomed view, (b) the deflected pose of meshed link.

2. Stiffness modeling methods

The stiffness methods can be classified as lumped and distributed modeling approaches. Here, lumped means that all of the stiffness information is lumped on a single node. In the distributed approach, the stiffness information is distributed among the many discrete elements of a body. Widely used distributed modeling approaches are FEM and Matrix Structural Method (MSM), while an extensively used lumped modeling approach is VJM. Strain Energy Method (SEM) is a computational approach that may be used with both distributed and lumped methods. In the following subsections, the main characteristics of each method are outlined briefly.

Stiffness modeling in the literature generally considers links as the only flexible bodies. Some studies also consider the joint stiffness [22,23]. Of course, joint stiffness plays a significant role in the stiffness model. However, this study is a comparison of FEM and VJM in terms of computation time and accuracy. Hence, we have excluded the joint stiffness in both methods for a fair comparison between them.

2.1. Finite element method

In this modeling technique, each body is decomposed into small discrete elements. The procedure is called “meshing”. A meshed link and the nodes on each element are illustrated in Fig. 2. The compliant deflections are computed concerning the applied force/torque vector, $\vec{F}$. This force vector is mapped on each node as $\bar{F}_\theta$. The overall deflection is computed by the accumulation of the small deflections of each node. The force/torque equilibrium and the deflection on a node are given by:

$$\begin{bmatrix} \bar{F}_{\theta i} \\ \bar{F}_{\theta i+1} \end{bmatrix} = \begin{bmatrix} \boldsymbol{K}_{\theta 11}^{(i)} & \boldsymbol{K}_{\theta 12}^{(i)} \\ \boldsymbol{K}_{\theta 21}^{(i+1)} 1 & \boldsymbol{K}_{\theta 22}^{(i+1)} \end{bmatrix} \begin{bmatrix} \Delta\bar{\theta}_i \\ \Delta\bar{\theta}_{i+1} \end{bmatrix} \tag{2.1}$$

where i denotes the computed nodes on elements. θ denotes the variables that are computed in the local frame of nodes. $\Delta\bar{\theta}$ is the deflections of the nodes, and $\boldsymbol{K}_\theta$ is a 6×6 stiffness matrix.

Complex shaped bodies can be easily meshed via FEM. Hence, the FEM gives accurate results regardless of the geometry of the link. However, the computation of the total deflection is an iterative process. Considering a high number of meshes, it takes a long time to obtain the solution for a single $\vec{F}$ value at a single configuration. In each configuration change, all bodies are re-meshed. This process extends the computation time [24]. Hence, a FEM approach is not suitable for real-time control and design optimization. However, FEM is preferred in the verification of the final design of an optimized manipulator [25]. The merits of the method are explained in [26] and studies on computation of stiffness via FEM are presented in [27–31].

2.2. Matrix structural method

MSM uses an analytical stiffness model that is derived through the Euler–Bernoulli approach. In MSM, a flexible link structure is modeled by using a number of simple structural elements like beams and tubes [32,33]. The method is illustrated for a single link in Fig. 3.

In [24], this method is applied to model a tripod-based parallel mechanism. Li et al. [34] obtained the stiffness model of a Stewart platform. Deblaise et al. [35] obtained a Delta-type parallel mechanism’s stiffness model. This method is also adopted in recent studies presented in [14,36–38], which indicates that this method is still extensively implemented in stiffness modeling of mechanisms.

Larger discrete elements are used in MSM relative to FEM. Each link is denoted by a 12×12 stiffness matrix. Hence, MSM is relatively simpler and faster compared to FEM. However, the method still requires long computation since it consists of

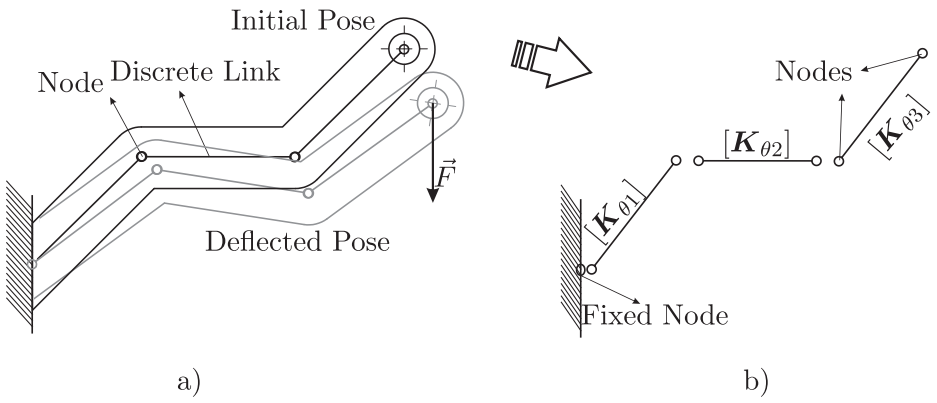

Fig. 3. MSM model of a link: (a) MSM model discretization, (b) the discrete elements which are defined via $[\boldsymbol{K}_\theta]_{12\times 12}$ local stiffness matrices.

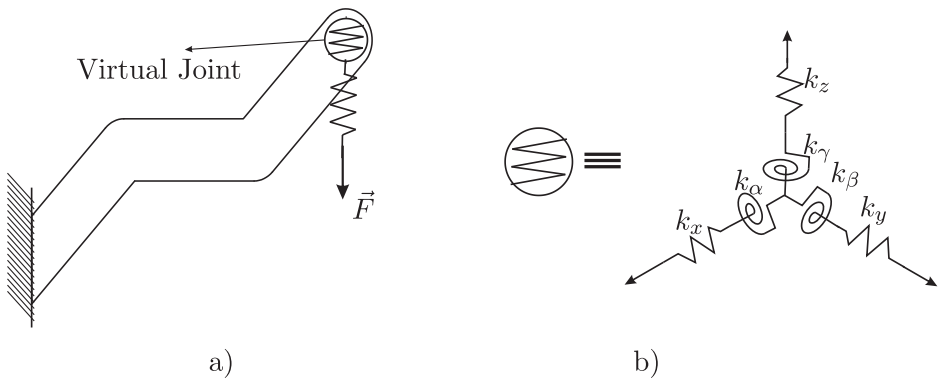

Fig. 4. VJM modeling of a link: (a) the VJM model, (b) virtual springs defined at the tip of link and a diagonal stiffness matrix $[\boldsymbol{K}_\theta]_{6\times 6} = \text{diag}(k_x, k_y, k_z, k_\alpha, k_\beta, k_\gamma)$ may be defined.

higher dimension matrices [28,38]. For instance, in a recent study, 10ms computation time is achieved [39] by using MSM for a planar parallel manipulator's stiffness model computation. The approach is considerably faster than a standard FEM simulation duration. However, with this computation time, the 1 kHz sampling frequency cannot be achieved in a haptic control loop. Therefore, MSM is not suitable for real-time haptic device control, but it may be used in the optimization process.

2.3. Virtual joint method

In this method, Jacobian matrices and the virtual work principle are used. In VJM, stiffness information of the links is lumped on virtual springs. These springs are placed on the virtual joints that are located at the distal end of each link. This distal end is either the location of the passive or active joint. Hence, the same virtual joint can be used to lump the passive/active joint stiffness information. A stiffness matrix of a link is given by a 6×6 stiffness matrix in VJM. Hence, a VJM model contains relatively smaller number of nodes in its calculation. Therefore, VJM is expected to be computationally more efficient when compared to MSM and FEM. In Fig. 4, the approach is illustrated by showing a 6 degrees of freedom (DOF) virtual joint with 6 virtual springs at the distal end of a single link. It is assumed that the deflections are small enough to construct the following equation:

$$\Delta\bar{X} \approx \boldsymbol{J}_\theta \Delta\bar{\theta} \tag{2.2}$$

where $\Delta\bar{X}$ is the change in position vector of the end-effector, $\Delta\bar{\theta}$ is the change in virtual joint variables, and $\boldsymbol{J}_\theta$ is the Jacobian matrix containing virtual joint variables. Consequently, the force/torque equilibrium of compliant manipulator is established as follows:

$$\bar{F}_{ext} = \boldsymbol{K}_C \Delta\bar{X} \tag{2.3}$$

$$\boldsymbol{K}_C = (\boldsymbol{J}_\theta \boldsymbol{K}_\theta^{-1} \boldsymbol{J}_\theta^T)^{-1} \tag{2.4}$$

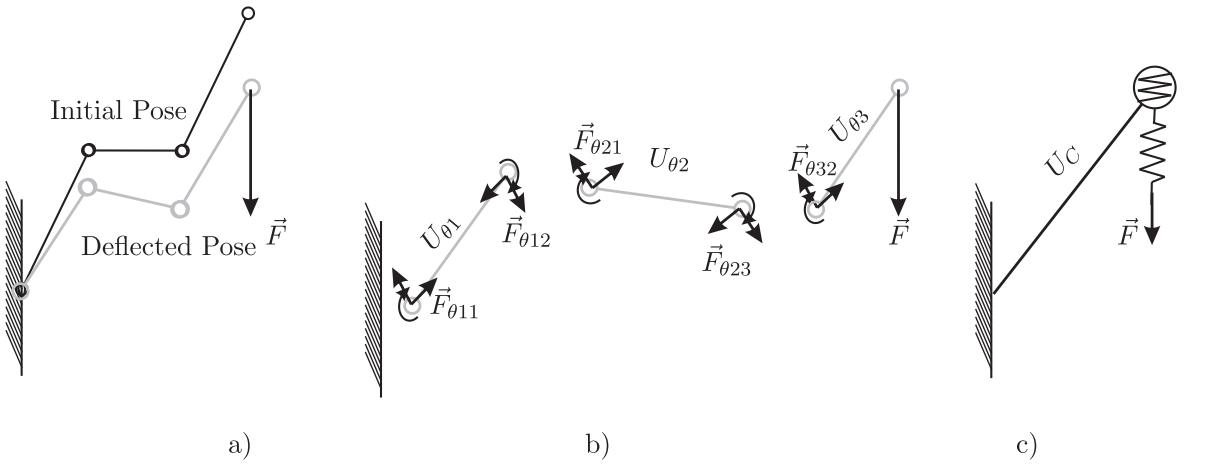

Fig. 5. SEM using distributed and lumped approach: (a) the MSM-SEM, (b) the stored energy U_θ of each link and forces/torques $\vec{F}_\theta$ in MSM, (c) the VJM-SEM and the total stored energy U_C.

where $\bar{F}_{ext}$ is the vector of applied wrenches on end-effector in task-space. $\boldsymbol{K}_C$ is the task-space stiffness matrix of the manipulator. $\boldsymbol{K}_\theta$ is the joint-space stiffness matrix.

In this method, either the applied forces $\bar{F}_{ext}$ or resultant deflections $\Delta\bar{X}$ are assumed to be known. $\boldsymbol{K}_\theta$ may be computed by using the analytical representations of beams [28,40,41], by using numerical results of FEM [42], or by using experimental results [43]. Therefore, while VJM produces computationally efficient models, these models can also produce reliable results.

Intially, the idea of the virtual joints was introduced by Salisbury and Craig [44]. Then, the concept was extended for parallel mechanisms by Gosselin [17]. Later, the method is improved for parallel manipulators as their compliant links are denoted by one dimensional linear and torsional springs [45]. In [28], VJM is further improved by including the influence of passive joints in the calculation of stiffness model for parallel mechanisms. Some relatively recent studies using VJM are presented in [46,47].

The reasons for selecting this method in this study are as follows:

- It permits a systematic approach in stiffness modeling of parallel manipulators,
- It can easily be modified with the results of FEM and experimental studies [48],
- It may be optimized to be fast enough for use in a real-time control loop and design optimization.

2.4. Strain energy method

SEM is a computation approach for lumped and distributed models. Elastic potential energy stored in the compliant bodies are investigated in this method [15]. If the stored energy is known, the compliant displacements can be computed assuming that there is no permanent shape deformation. Castigliano's theorem [49–51] is used in this method, and the stiffness matrix is obtained by computing the Hessian matrix of the potential energy [52] as follows:

$$U_C = \frac{1}{2}\Delta\bar{F}_{ext}^T \boldsymbol{C}_C \Delta\bar{F}_{ext}, \quad \boldsymbol{C}_C = \frac{\partial^2 U}{\partial \bar{F}_{ext}^2} \tag{2.5}$$

$$U_\theta = \frac{1}{2}\Delta\bar{F}_\theta^T \boldsymbol{C}_\theta \Delta\bar{F}_\theta, \quad \boldsymbol{C}_\theta = \frac{\partial^2 U_\theta}{\partial \bar{F}_\theta^2} \tag{2.6}$$

where U_C and U_θ are the strain energies that are obtained in terms of Cartesian space and joint-space variables, respectively. Note that, $U_C = U_\theta$. $\boldsymbol{C}_C$ and $\boldsymbol{C}_\theta$ are the compliance matrices defined in Cartesian space and joint space, respectively. $\bar{F}_{ext}$ and $\bar{F}_\theta$ are the force/torque vectors denoted in the Cartesian space and joint space, respectively (see Fig. 5).

The drawback of the approach is the difficulty in obtaining an analytic representation. It becomes a significant problem when links cannot be represented by simple structures like beams and tubes. This method is employed in [53] for a 6-DOF parallel mechanism. In [54], a parallelogram-type parallel mechanism's stiffness model is obtained and compared with the FEM results. In [30], a general approach for SEM-based stiffness modeling is proposed for over-constrained parallel mechanisms with SCARA motion, and in [31], this method is applied for over-constrained parallel mechanisms.

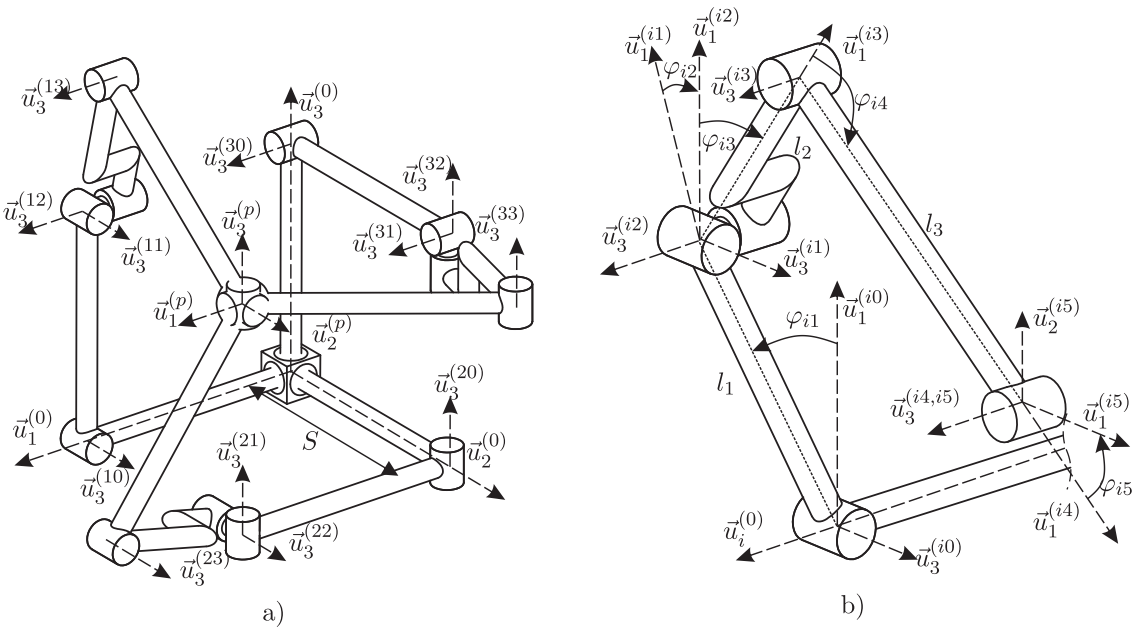

Fig. 6. Kinematic sketches of the R-CUBE mechanism [13]: (a) The manipulator, (b) variables of *i*th serial chain where *i* is one of the serial chains.

3. A case study on an R-CUBE mechanism

3.1. Kinematics model

R-CUBE manipulator is introduced in [20] with two different structural designs. The active linkage group is determined as a parallelogram in one of its design. In the other design, a single link is used as the active link. In this study, we focus on the design solution without the parallelograms since it has relatively fewer moving parts, which result in smaller moving inertia and a smaller number of joints. These are beneficial in a haptic application to minimize the impedance mechanical characteristics. Moreover, the single link version requires less computational costs for stiffness modeling as compared with parallelograms. This manipulator has 3 translational DOF at its mobile platform with a decoupled motion structure. The actuated links are attached to the base. They are connected to a mobile platform via 2R passive serial kinematic chains. In Fig. 6, a sketch that provides information on the kinematics of the R-CUBE mechanism is illustrated.

In Fig. 6, initial frame of *k*th serial chain is located on $\vec{u}_k^{(0)}$ unit vector where $k = 1, 2, 3$. $\vec{u}_k^{(ij)}$ indicates the unit vector belonging to the *j*th frame of the *i*th serial chain. $\vec{u}_k^{(0)} \parallel \vec{u}_k^{(p)}$ where p is the frame of the mobile platform. Kinematic constraints align $\vec{u}_3^{(15)}, \vec{u}_3^{(25)}, \vec{u}_3^{(35)}$ with $\vec{u}_1^{(35)}, \vec{u}_1^{(15)}, \vec{u}_1^{(25)}$ vectors, respectively. Note that, dimensions of the mobile platform do not change the coordinates of the mobile platform frame because the origin of this frame is defined at the intersection point of $\vec{u}_k^{(p)}$ vectors for $k = 1, 2, 3$. In this case, the forward kinematics is represented by a single equation as follows:

$$r_i = S + l_1 \sin\varphi_{i1} \quad \text{for } i = 1, 2, 3 \quad \text{and} \quad \bar{r} = \begin{bmatrix} r_1 & r_2 & r_3 \end{bmatrix}^T \tag{3.1}$$

where S is a constant distance between the origin and $\vec{u}_3^{(i0)}$. l_1 is a common link length for all the serial kinematic chains' first link. $\bar{r}$ denotes the position of the mobile platform with respect to the origin.

3.2. VJM stiffness model

VJM model of the R-CUBE mechanism is derived by implementing the virtual joint variables into the compliant kinematics formulations. In a general format, a virtual joint can be defined as follows [19]:

$$\boldsymbol{H}_v(\bar{\theta}_{ij}) = \boldsymbol{T}_1(\theta_{ij}^1)\boldsymbol{T}_2(\theta_{ij}^2)\boldsymbol{T}_3(\theta_{ij}^3)\boldsymbol{R}_1(\theta_{ij}^4)\boldsymbol{R}_2(\theta_{ij}^5)\boldsymbol{R}_3(\theta_{ij}^6) \tag{3.2}$$

where $\boldsymbol{H}_v$ denotes the homogeneous transformation matrix for virtual joints and $\bar{\theta}_{ij}$ is the column matrix containing virtual joint variables of the *j*th body in the *i*th serial chain. $\boldsymbol{R}_k$ and $\boldsymbol{T}_k$ are homogeneous transformation matrices for pure rotation and pure translation where k denotes the rotation/translation axis for $k = 1, 2, 3$. Superscripts of θ_{ij} denote element number in $\bar{\theta}_{ij}$. A sketch of R-CUBE's compliant kinematics is illustrated in Fig. 7.

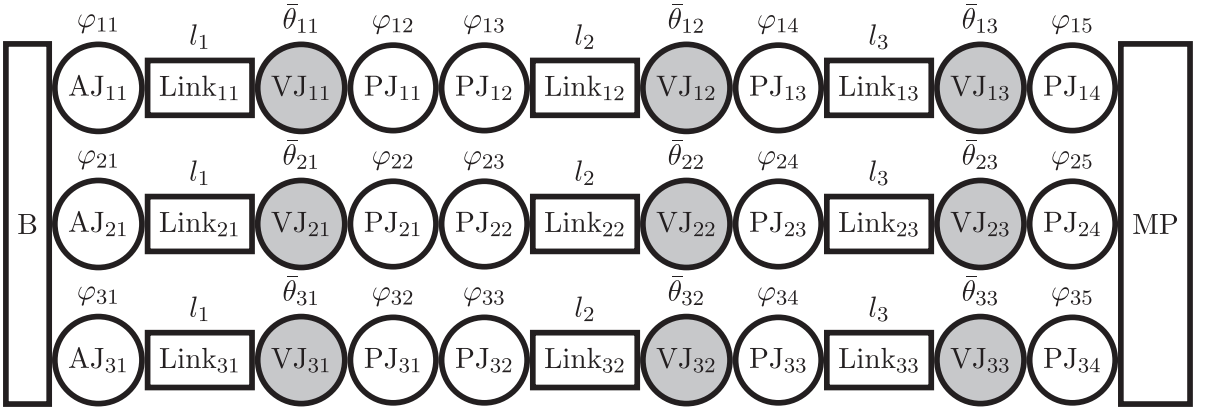

Fig. 7. Compliant kinematics of the manipulator and its virtual joint model where AJ is active joint, PJ is passive joint, VJ is virtual joint, MP is mobile platform, B is base.

The mathematical model for compliant forward kinematics of the *i*th serial chain is represented by Eqs. (3.3) to (3.8). Since all three serial kinematic chains are connected to each other at a single point on the mobile platform, the total homogeneous transformation matrices calculated for all serial chains are equal to each other as shown in Eq. (3.9).

$$\boldsymbol{H}^{(i0,K_{i1})} = \boldsymbol{R}_3(\varphi_{i1})\boldsymbol{T}_1(l_1)\boldsymbol{H}_v(\bar{\theta}_{i1}) \tag{3.3}$$

$$\boldsymbol{H}^{(K_{i1},K_{i2})} = \boldsymbol{R}_3(\varphi_{i2})\boldsymbol{R}_1(-\pi/2)\boldsymbol{R}_3(\varphi_{i3})\boldsymbol{T}_1(l_2)\boldsymbol{H}_v(\bar{\theta}_{i2}) \tag{3.4}$$

$$\boldsymbol{H}^{(K_{i2},K_{i3})} = \boldsymbol{R}_3(\varphi_{i4})\boldsymbol{T}_1(l_3)\boldsymbol{H}_v(\bar{\theta}_{i3}) \tag{3.5}$$

$$\boldsymbol{H}^{(K_{i3},i5)} = \boldsymbol{R}_3(\varphi_{i5}) \tag{3.6}$$

$$\boldsymbol{H}_{Ki} = \boldsymbol{H}^{(0,i0)}\boldsymbol{H}^{(i0,K_{i1})}\boldsymbol{H}^{(K_{i1},K_{i2})}\boldsymbol{H}^{(K_{i2},K_{i3})}\boldsymbol{H}^{(K_{i3},i5)}\boldsymbol{H}^{(i5,p)} \tag{3.7}$$

$$\boldsymbol{H}_{Ki} = \begin{bmatrix} \boldsymbol{R}_{Ki} & \bar{r}_{Ki} \\ \bar{0}^T & 1 \end{bmatrix} \tag{3.8}$$

$$\boldsymbol{H}_{K1} = \boldsymbol{H}_{K2} = \boldsymbol{H}_{K3} \tag{3.9}$$

where $\boldsymbol{R}_{Ki}$ and $\bar{r}_{Ki}$ denote the rotation and position matrices of the mobile platform including the virtual joints. $\boldsymbol{H}_{Ki}$ is the homogeneous transformation matrix containing the active, passive, and virtual joint variables. Under external wrenches, compliant displacements calculated from each serial chain should be equal to each other such that $\Delta\boldsymbol{H}_{K1} = \Delta\boldsymbol{H}_{K2} = \Delta\boldsymbol{H}_{K3}$ assuming that the mobile platform is rigid. Since the mobile platform is considered to be rigid, its dimensions do not affect the stiffness model. However, the offsets of the mobile platform should be considered if the external force/torque vector is not applied at the origin of the mobile platform frame.

The joint variables are presented in column matrix form as follows:

$$\bar{q}_{pi} = \begin{bmatrix} \varphi_{i2} & \varphi_{i3} & \varphi_{i4} & \varphi_{i5} \end{bmatrix}^T_{4\times1}, \quad \bar{q}_i = \varphi_{i1} \tag{3.10}$$

$$\bar{\theta}_i = \begin{bmatrix} \bar{\theta}_{i1}^T & \bar{\theta}_{i2}^T & \bar{\theta}_{i3}^T \end{bmatrix}^T_{18\times1} \tag{3.11}$$

$$\bar{Q}_i = \begin{bmatrix} \bar{\theta}_i^T & \bar{q}_{pi}^T & q_{i1} \end{bmatrix}^T_{23\times1} \tag{3.12}$$

where $\bar{Q}_i$ contains all joint variables for the *i*th serial chain. By making use of general notation of $\bar{Q}_i$. Jacobian matrix can be procured for all joint variables including active, passive, and virtual ones.

$$\frac{\partial \boldsymbol{H}_{Ki}}{\partial Q_{ik}} = \begin{bmatrix} \frac{\partial \boldsymbol{R}_{Ki}}{\partial Q_{ik}} & \frac{\partial \bar{r}_{Ki}}{\partial Q_{ik}} \\ \bar{0}^T & 1 \end{bmatrix} \text{ for } k = 1, 2, \ldots, 23 \tag{3.13}$$

where subscript k denotes the k^{th} variable of $\bar{Q}_i$.

Angular velocity coefficients are obtained by using the derivative of the rotation matrix. $\tilde{\Omega}_{ik}$ is a skew-symmetric matrix which contains the angular velocity coefficients. By using the *col* operator, angular velocity coefficients are obtained in a column matrix format Eq. (3.14). Linear velocity coefficients in column matrix form $\bar{V}_{ik}$ are obtained by differentiating $\bar{r}_{Ki}$ with respect to the Q_{ik}th variable as shown in Eq. (3.15). Finally, 6×1 column Jacobian matrix, $\bar{J}_{Kik}$, of Q_{ik}th variables are

formed as shown in Eq. (3.16).

$$\tilde{\Omega}_{ik} = \frac{\partial \boldsymbol{R}_{Ki}}{\partial Q_{ik}} \boldsymbol{R}_{Ki}^{T} = \begin{bmatrix} 0 & -\Omega ik_3 & \Omega ik_2 \\ \Omega ik_3 & 0 & -\Omega ik_1 \\ -\Omega ik_2 & \Omega ik_1 & 0 \end{bmatrix}, \quad \bar{\Omega}_{ik} = col(\tilde{\Omega}_{ik}) = \begin{bmatrix} \Omega ik_1 & \Omega ik_2 & \Omega ik_3 \end{bmatrix}^{T} \tag{3.14}$$

$$\bar{V}_{ik} = \frac{\partial \bar{r}_{Ki}}{\partial Q_{ik}} \tag{3.15}$$

$$\bar{J}_{Kik} = \begin{bmatrix} \bar{V}_{ik}^{T} & \bar{\Omega}_{ik}^{T} \end{bmatrix}^{T} \tag{3.16}$$

The Jacobian matrix $\boldsymbol{J}_{Ki}$ containing active, passive, and virtual joints for the ith serial chain is formulated by using the column matrices that are mentioned above. It is then divided into sub-Jacobian matrices as $\boldsymbol{J}_{\theta i}$, $\boldsymbol{J}_{pi}$, and $\bar{J}_{ai}$ that are obtained by differentiation with respect to the virtual joints, passive joints, and active joint, respectively.

$$\boldsymbol{J}_{\theta i} = \begin{bmatrix} \bar{J}_{Ki1} & \bar{J}_{Ki2} & \cdots & \bar{J}_{Ki18} \end{bmatrix}_{6\times 18} \tag{3.17}$$

$$\boldsymbol{J}_{pi} = \begin{bmatrix} \bar{J}_{Ki19} & \bar{J}_{Ki20} & \bar{J}_{Ki21} & \bar{J}_{Ki22} \end{bmatrix}_{6\times 4} \tag{3.18}$$

$$\bar{J}_{ai} = \begin{bmatrix} \bar{J}_{Ki23} \end{bmatrix}_{6\times 1} \tag{3.19}$$

$$\boldsymbol{J}_{Ki} = \begin{bmatrix} \boldsymbol{J}_{\theta i} & \boldsymbol{J}_{pi} & \bar{J}_{ai} \end{bmatrix}_{6\times 23} \tag{3.20}$$

Based on the assumption presented in (2.2), obtained Jacobian matrices are used to calculate the compliant deflections of the mobile platform as follows:

$$\Delta \bar{X}_i = \boldsymbol{J}_{Ki} \Delta \bar{Q}_i \tag{3.21}$$

$$\Delta \bar{X}_i = \boldsymbol{J}_{\theta i} \Delta \bar{\theta}_i + \boldsymbol{J}_{pi} \Delta \bar{q}_{pi} + \bar{J}_{ai} \Delta q_{i1} \tag{3.22}$$

where $\Delta \bar{X}_i$ is 6×1 column matrix containing translational and rotational compliant deflections of the last frame of the ith serial chain. Δ operator denotes the change in conditions between loaded and unloaded states.

$\boldsymbol{J}_{Ki}$ in Eq. (3.21) is used for mapping external wrenches in Cartesian space to joint-space forces/torques as follows:

$$\bar{F}_{Ki} = \boldsymbol{J}_{Ki}^{T} \bar{F}_{ext} \tag{3.23}$$

where $[\bar{F}_{Ki}]_{23\times 1}$ is the joint-space force/torque vector for virtual, passive, and active joints, respectively. $[\bar{F}_{ext}]_{6\times 1}$ is the external wrench including three-dimensional forces and moments. $\bar{F}_{Ki}$ can be divided into 3 sub-components, and the force/torque vector of each joint are calculated as follows:

$$\bar{F}_{Ki} = \begin{bmatrix} \bar{F}_{\theta i}^{T} & \bar{F}_{pi}^{T} & \bar{F}_{ai}^{T} \end{bmatrix}^{T} = \begin{bmatrix} \boldsymbol{J}_{\theta i} & \boldsymbol{0} & \bar{0} \end{bmatrix}^{T} \bar{F}_{ext} + \begin{bmatrix} \boldsymbol{0} & \boldsymbol{J}_{pi} & \bar{0} \end{bmatrix}^{T} \bar{F}_{ext} + \begin{bmatrix} \boldsymbol{0} & \boldsymbol{0} & \bar{J}_{ai} \end{bmatrix}^{T} \bar{F}_{ext} \tag{3.24}$$

where $[\bar{F}_{\theta i}]_{18\times 1}$, $[\bar{F}_{pi}]_{4\times 1}$, and $[F_{ai}]_{1\times 1}$ are the joint-space force/torque for virtual, passive, and active joints, respectively.

$\bar{F}_{Ki}$ is functions of the stiffness matrices and deflections in joint-space.

$$\bar{F}_{Ki} = diag(\boldsymbol{K}_{\theta i}, \boldsymbol{K}_{pi}, K_{ai}) \Delta \bar{Q}_i \tag{3.25}$$

$$\boldsymbol{K}_{\theta i} = diag(\boldsymbol{K}_{\theta i1}, \boldsymbol{K}_{\theta i2}, \boldsymbol{K}_{\theta i3})_{18\times 18} \tag{3.26}$$

$$\boldsymbol{K}_{\theta ik} = \begin{bmatrix} EA_k/l_k & 0 & 0 & 0 & 0 & 0 \\ 0 & 12EI_{zk}/l_k^3 & 0 & 0 & 0 & -6EI_{zk}/l_k^2 \\ 0 & 0 & 12EI_{yk}/l_k^3 & 0 & 6EI_{yk}/l_k^2 & 0 \\ 0 & 0 & 0 & GJ_k/l_k & 0 & 0 \\ 0 & 0 & 6EI_{yk}/l_k^2 & 0 & 4EI_{yk}/l_k & 0 \\ 0 & -6EI_{zk}/l_k^2 & 0 & 0 & 0 & 4EI_{zk}/l_k \end{bmatrix} \tag{3.27}$$

where A_k, I_{zk}, I_{yk} are the area and the second moments of the link cross-section area. E_k and G_{xyk} are the Young and Coulomb modulus of the link material. J_k is the polar moment. Sub-script k denotes the kth link. $\boldsymbol{K}_{\theta i}$ denotes the structural stiffness matrix of a single serial chain in joint-space. $\boldsymbol{K}_{\theta ik}$ for $k = 1, 2, 3$ denotes each respective link's stiffness matrix. Consequently, the size of $\boldsymbol{K}_{\theta i}$ is 18×18. $\boldsymbol{K}_{pi}$ and K_{ai} denote the 4×4 stiffness matrix for passive joints and stiffness coefficient for active joint.

Eq. (3.25) is rearranged in Cartesian space by making use of Eqs. (3.23) and (3.21).

$$\boldsymbol{J}_{Ki}^{T} \bar{F}_{ext} = diag(\boldsymbol{K}_{\theta i}, \boldsymbol{K}_{pi}, K_{ai}) \Delta \bar{Q}_i \text{ and } \boldsymbol{J}_{Ki}^{-1} \Delta \bar{X}_i = \Delta \bar{Q}_i \tag{3.28}$$

$$\Rightarrow \bar{F}_{ext} = \boldsymbol{J}_{Ki}^{-T} diag(\boldsymbol{K}_{\theta i1}, \boldsymbol{K}_{\theta i2}, \boldsymbol{K}_{\theta i3}) \boldsymbol{J}_{Ki}^{-1} \Delta \bar{X}_i \tag{3.29}$$

When $\boldsymbol{J}_{Ki}$ is substituted to the above equation, the following equality is obtained.

$$\bar{F}_{ext} = (\boldsymbol{J}_{\theta i}^{-T}\boldsymbol{K}_{\theta i}\boldsymbol{J}_{\theta i}^{-1} + \boldsymbol{J}_{pi}^{-T}\boldsymbol{K}_{pi}\boldsymbol{J}_{pi}^{-1} + \bar{J}_{ai}^{-T}K_{ai}\bar{J}_{ai}^{-1})\Delta\bar{X}_i \tag{3.30}$$

$\Delta\bar{X}_i$ is the computed compliant displacement of the last frame of the ith serial chain. $\Delta\bar{q}_{pi} \neq \bar{0}$ since passive joints are free to rotate about their own axes with the assumption that the joint frictions can be neglected. It is assumed that active joints are locked to obtain information on the structural stiffness; hence, $\Delta q_{i1} = 0$. $\Delta\bar{\theta}_i = \bar{\theta}_i$ because in the initial condition there is no load on the system and $\bar{\theta}_i^{initial} = 0$. According to the previous assumptions and investigations, $\Delta\bar{X}_i$ in Eq. (3.22) is updated as follows:

$$\Rightarrow \Delta\bar{X}_i = \boldsymbol{J}_{\theta i}\bar{\theta}_i + \boldsymbol{J}_{pi}\Delta\bar{q}_{pi} \tag{3.31}$$

The above equality is substituted in Eq. (3.30) and it is simplified as:

$$\bar{F}_{ext} = (\boldsymbol{J}_{\theta i}^{-T}\boldsymbol{K}_{\theta i}\boldsymbol{J}_{\theta i}^{-1} + \boldsymbol{J}_{pi}^{-T}\boldsymbol{K}_{pi}\boldsymbol{J}_{pi}^{-1})\Delta\bar{X}_i \tag{3.32}$$

Since passive joints do not generate reaction torques in their rotation axes assuming that there is no friction, $\boldsymbol{K}_{pi} = \boldsymbol{0}$. Consequently, $\bar{F}_{Ki}$ only contains forces and torques of virtual joints. Therefore, Eq. (3.32) is further simplified in Eq. (3.33) and Eq. (3.34) is obtained. $\bar{\theta}_i$ is solved from Eq. (3.34).

$$\bar{F}_{ext} = (\boldsymbol{J}_{\theta i}^{-T}\boldsymbol{K}_{\theta i}\boldsymbol{J}_{\theta i}^{-1})\Delta\bar{X}_i \tag{3.33}$$

$$\bar{F}_{ext} = \boldsymbol{J}_{\theta i}^{-T}\boldsymbol{K}_{\theta i}\bar{\theta}_i \tag{3.34}$$

$$\boldsymbol{J}_{pi}^{T}\bar{F}_{ext} = \bar{0} \tag{3.35}$$

The structural stiffness matrix $\boldsymbol{K}_{Ci}$ is defined in Eq. (3.33).

$$\boldsymbol{K}_{Ci} = (\boldsymbol{J}_{\theta i}^{-T}\boldsymbol{K}_{\theta i}\boldsymbol{J}_{\theta i}^{-1})_{6\times 6} \tag{3.36}$$

However, this calculation omits the effects of passive joints. Therefore, $\text{rank}(\boldsymbol{K}_{Ci}) = 6$ of the above matrix. Since passive joints are free to rotate, they decrease the rank of stiffness matrix $\boldsymbol{K}_{Ci}$. This effect is included by constructing the following homogeneous relation matrix by using Eqs. (3.33) and (3.35).

$$\begin{bmatrix} (\boldsymbol{J}_{\theta i}\boldsymbol{K}_{\theta i}^{-1}\boldsymbol{J}_{\theta i}^{T}) & \boldsymbol{J}_{pi} \\ \boldsymbol{J}_{pi}^{T} & \boldsymbol{0} \end{bmatrix}\begin{bmatrix} \bar{F}_{ext} \\ \Delta\bar{q}_{pi} \end{bmatrix} = \begin{bmatrix} \Delta\bar{X}_i \\ \bar{0} \end{bmatrix} \tag{3.37}$$

Taking the inverse of the matrix that is on the left-hand side of Eq. (3.37) produces a rank deficient $\boldsymbol{K}_{Ci}$ matrix. The homogeneous relation matrix is invertible if $\det(\boldsymbol{J}_{\theta i}^{T}\boldsymbol{J}_{\theta i}) \neq 0$. The inversion is shown as follows:

$$\begin{bmatrix} (\boldsymbol{J}_{\theta i}\boldsymbol{K}_{\theta i}^{-1}\boldsymbol{J}_{\theta i}^{T}) & \boldsymbol{J}_{pi} \\ \boldsymbol{J}_{pi}^{T} & \boldsymbol{0} \end{bmatrix}^{-1} = \left[\begin{array}{c|c} [\boldsymbol{K}_{Ci}]_{6\times 6} & \sim \\ \hline \sim & \sim \end{array}\right] \tag{3.38}$$

where upper-left 6×6 sub-part of the above inversion contains the desired modified $\boldsymbol{K}_{Ci}$ matrix.

$\boldsymbol{K}_{Ci}$ matrices are summed up in order to obtain the Cartesian stiffness matrix as if they are springs connected in parallel to the mobile platform as shown in Eq. (3.39).

$$\boldsymbol{K}_C = \sum_{i=1}^{3}\boldsymbol{K}_{Ci} \tag{3.39}$$

If there is no external wrench on the mobile platform ($\bar{F}_{ext} = \bar{0}$), $\boldsymbol{K}_C$ takes the following form in Eq. (3.40). For small deflections and loads, this matrix can be used without resulting in large errors. If $|\bar{F}_{ext}| >> 0$, an iterative approach should be used and $\boldsymbol{K}_C$ must be recomputed for each iteration.

$$\boldsymbol{K}_C = \begin{bmatrix} K_{C_1}^{(11)} & 0 & 0 & 0 & K_{C_1}^{(15)} & K_{C_1}^{(16)} \\ 0 & K_{C_2}^{(22)} & 0 & K_{C_2}^{(24)} & 0 & K_{C_2}^{(26)} \\ 0 & 0 & K_{C_3}^{(33)} & K_{C_3}^{(34)} & K_{C_3}^{(35)} & 0 \\ 0 & K_{C_2}^{(24)} & K_{C_3}^{(34)} & K_{C_2}^{(44)} + K_{C_3}^{(44)} & K_{C_3}^{(45)} & K_{C_2}^{(46)} \\ K_{C_1}^{(15)} & 0 & K_{C_3}^{(35)} & K_{C_3}^{(45)} & K_{C_1}^{(55)} + K_{C_3}^{(55)} & K_{C_1}^{(56)} \\ K_{C_1}^{(16)} & K_{C_2}^{(26)} & 0 & K_{C_2}^{(46)} & K_{C_1}^{(56)} & K_{C_1}^{(66)} + K_{C_2}^{(66)} \end{bmatrix} \tag{3.40}$$

Units of the elements of $\boldsymbol{K}_C$ are illustrated by re-organizing this matrix as 3×3 sub-matrices in Eq. (3.41).

$$\boldsymbol{K}_C = \begin{bmatrix} \boldsymbol{K}_{CA} & \boldsymbol{K}_{CB} \\ \boldsymbol{K}_{CC} & \boldsymbol{K}_{CD} \end{bmatrix} \tag{3.41}$$

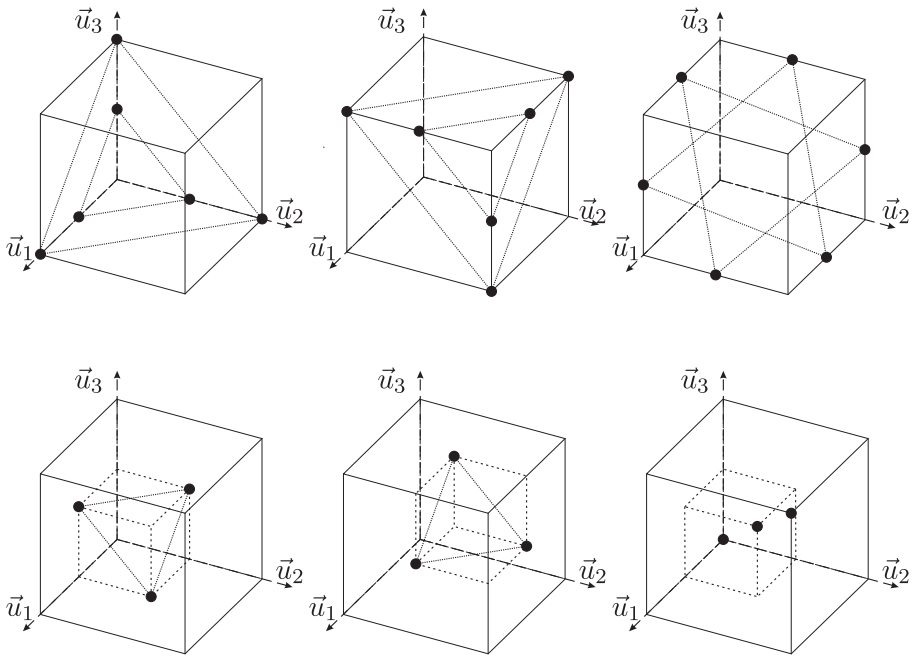

Fig. 8. Significant locations in the workspace. Black circles denote these poses. Solid lines that connect these poses show that they are kinematically symmetric.

where $\boldsymbol{K}_{CA}$, $\boldsymbol{K}_{CB}$, $\boldsymbol{K}_{CC}$, and $\boldsymbol{K}_{CD}$ have the units of *N/m, N/rad, N/rad*, and *Nm*, respectively.

In this study, it is assumed that the applied wrenches are known. This is an accurate assumption for a haptic scenario since the actuators are used to reflect desired/calculated resistance forces to the user. Since the wrenches are known, the compliance matrix is computed to obtain compliant displacements. The compliance matrix, $\boldsymbol{C}_C$, and its sub-components are given as follows:

$$\boldsymbol{C}_C = \boldsymbol{K}_C^{-1} = \begin{bmatrix} \boldsymbol{C}_{CA} & \boldsymbol{C}_{CB} \\ \boldsymbol{C}_{CC} & \boldsymbol{C}_{CD} \end{bmatrix} \tag{3.42}$$

where $\boldsymbol{C}_{CA}$, $\boldsymbol{C}_{CB}$, $\boldsymbol{C}_{CC}$, and $\boldsymbol{C}_{CD}$ have the units of *m/N, rad/N, rad/N*, and $(Nm)^{-1}$, respectively. Compliant deflections are computed as:

$$\Delta\vec{X} = \boldsymbol{C}_C\vec{F}_{ext}. \tag{3.43}$$

4. Simulation setup

The manipulator has the maximum/minimum kinematic, stiffness, or dynamic performances at some poses. These poses are critical poses that contain important information about the manipulator. These configurations turn out to be the ones when the active links are fully folded, fully extended, and in their home position. In its current optimized design of the R-CUBE mechanism, the maximum range of active joint variables is limited between $\pm 30^\circ$. This generates 27 poses for $\pm 30^\circ$ and 0° for each active joint variable. The locations of these poses in the workspace are shown in Fig. 8 and an example location set is given in Fig. 9(a) to illustrate the poses of a random selection of active joint positions. 10 active joint position combinations were selected to identify the test poses (TPs). These poses provide sufficient information for stiffness model verification thanks to the symmetric architecture of the manipulator. The selected TPs are presented in Table 1 and shown in Fig. 9(b).

The manipulator was designed to display three-dimensional forces to the user in a haptic scenario. In addition, the prototype has a passive spherical joint that connects the handle on the mobile platform. Also, the rotation center of the

Table 1
Active joint values of TPs, **TP=TP(q_{11}, q_{21}, q_{31})**, $-30 \Rightarrow -30^\circ$, $+30 \Rightarrow +30^\circ$, $0 \Rightarrow 0^\circ$.

Active joint variables	TP1	TP2	TP3	TP4	TP5	TP6	TP7	TP8	TP9	TP10
q_{11}	−30	0	+30	0	0	0	0	+30	+30	0
q_{21}	−30	0	+30	0	0	+30	−30	−30	−30	−30
q_{31}	−30	0	+30	+30	−30	+30	−30	−30	+30	+30

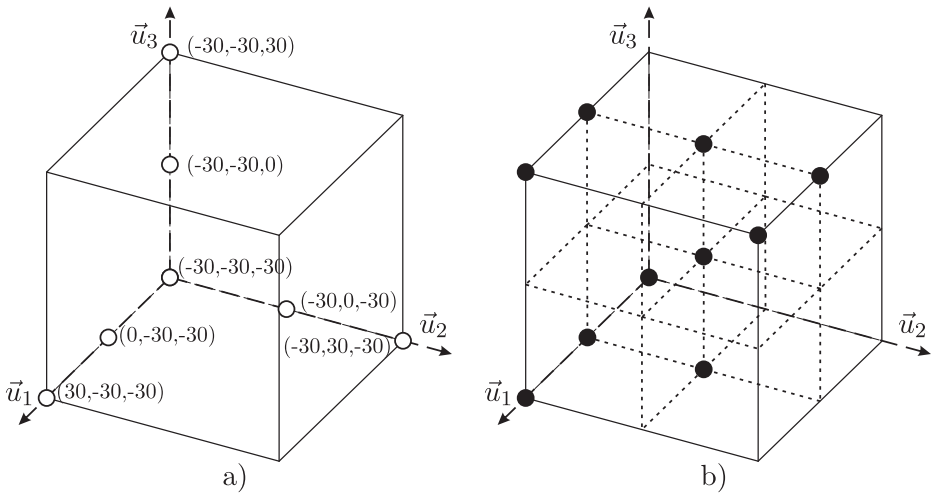

Fig. 9. Locations in the workspace: (a) example locations of the mobile platform for a randomly selected active joint angle set, (b) locations of selected TPs.

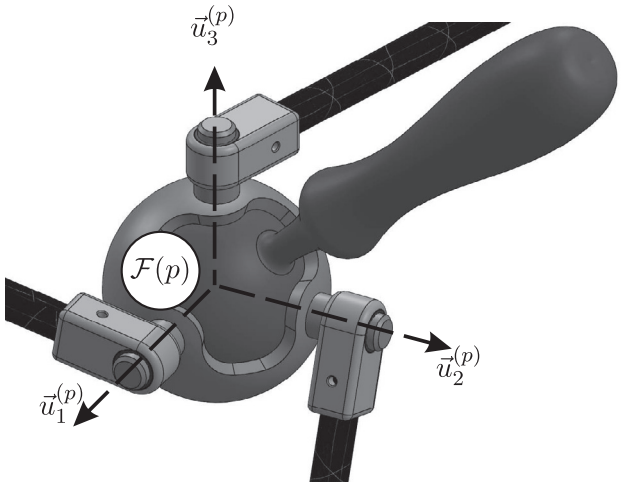

Fig. 10. CAD sketch of the mobile platform.

spherical joint is coincident with the mobile platform frame. Hence, it is not possible to induce external moments to the mobile platform. A sketch of a possible design of the mobile platform is illustrated in Fig. 10. In this way, the intersection of the axes of the revolute joints that connect the serial chains to the mobile platform is aligned with the center of the ball-in-socket joint, which is used to mount the handle to the mobile platform. Hence, neglecting the moments due to the frictions in the ball-in-socket joint, only external three-dimensional forces can be exerted on the mobile platform by the human operator. Even though the current design does not permit applying torsional loads, we have considered this kind of loading for verification purpose and the generality of the proposed approach. Hence, computed stiffness matrices are always 6×6, and therefore, computation time includes the time spent for computing the translational and rotational compliant displacements.

Forces and torques ranging between ± 5 N and ± 1 Nm are selected to be applied to the manipulator's mobile platform. The force range is the maximum force range of the designed haptic device. On the other hand, the range of torque input is considered as a unit input for verification purpose of the stiffness model. In a three dimensional space, it is possible to obtain 2^3 combinations of load for the proposed ranges. Hence, 8 loading combinations are possible for each loading type. Each combination is identified as a load combination (LC) in Table 2 for forces and Table 3 for torques. In VJM and FEM computations, gravitation and dynamic effects were excluded. The reason to exclude the dynamic effects is that the haptic device usually displays resistive forces to the user at a static condition such as the boundary of a virtual wall. A map of the compliant displacements due to the gravitational effects can be made for any location of the workspace. Thus, this information can be used as a bias in the overall compliant displacement calculation of the end-effector in order to decrease the overall computational cost of the stiffness model calculation.

Table 2
Magnitude of applied loads and load combinations of forces.

Direction	LC1	LC2	LC3	LC4	LC5	LC6	LC7	LC8
$\vec{u}_1^{(0)}$	+5 N	+5 N	+5 N	+5 N	−5 N	−5 N	−5 N	−5 N
$\vec{u}_2^{(0)}$	+5 N	+5 N	−5 N	−5 N	+5 N	+5 N	−5 N	−5 N
$\vec{u}_3^{(0)}$	+5 N	−5 N	+5 N	−5 N	+5 N	−5 N	+5 N	−5 N

Table 3
Magnitude of applied loads and load combinations of torques.

Direction	LC1	LC2	LC3	LC4	LC5	LC6	LC7	LC8
$\vec{u}_1^{(0)}$	+1 Nm	+1 Nm	+1 Nm	+1 Nm	−1 Nm	−1 Nm	−1 Nm	−1 Nm
$\vec{u}_2^{(0)}$	+1 Nm	+1 Nm	−1 Nm	−1 Nm	+1 Nm	+1 Nm	−1 Nm	−1 Nm
$\vec{u}_3^{(0)}$	+1 Nm	−1 Nm	+1 Nm	−1 Nm	+1 Nm	−1 Nm	+1 Nm	−1 Nm

Several simulations were executed to compare FEM and VJM. Computations were conducted on the same computer to have a fair comparison. ANSYS Workbench was used for FEM computations. VJM model was constructed in MATLAB software. The same link structures were used in both models. R-CUBE mechanism's CAD model is shown in Fig. 11(a). Although it is relatively easy to obtain a FEM of this complex geometry, it is not easy to construct an exact VJM model due to the irregular shape of the links. Especially, the connection between the links and universal joints is relatively hard to implement in VJM. Since the main aim in this study is to have a fair comparison between the FEM and VJM in terms of computation time and accuracy of results, the link design was simplified to hollow tubes to be used in both models as shown in Fig. 11(b). The dimensions of the manipulator are the result of an optimal design process [55].

Hollow tube's inner and outer diameters are identical for each link. Material type of links was set as structural steel. The dimensions of the tubes and the material properties are given in Fig. 13. VJM model was obtained according to these dimensions and material properties. Configuration of the manipulator changes in each TP. Hence, a stiffness matrix must be obtained in each TP. Then, LCs should be applied to the models in both simulation environments. A solution algorithm for VJM model is given in Fig. 12 to represent the application of all LCs on all TPs.

The simplified CAD model was also implemented in an ANSYS Workbench simulation. The base structure was defined as a rigid body in the "Geometry" section of the "Static Structural" tool. The remaining bodies were set as elastic bodies. Then, orthogonal coordinate frames were defined at each tip of the links, as shown in Fig 14(a). Next, a "remote point" was defined on each coordinate frame. These remote points are body-fixed points, and they are constrained by the circular profile of hollow tube structure, as shown in Fig. 14(b). This relation is also preserved after the meshing process, as shown in Fig. 14(c). Hence, when the meshes are deformed under the load, the remote point and its reference frame also deform with the attached mesh structure. By observing each remote point, it is possible to obtain the translation and rotation information of all frames, including the mobile platform frame. The connection of the links was achieved via the remote points. These points were connected by using "Revolute" and "Universal" joint options. This connection is illustrated in Fig. 15 for a single serial chain. At the mobile platform frame, the last remote points of each serial chain intersect with each other. All last

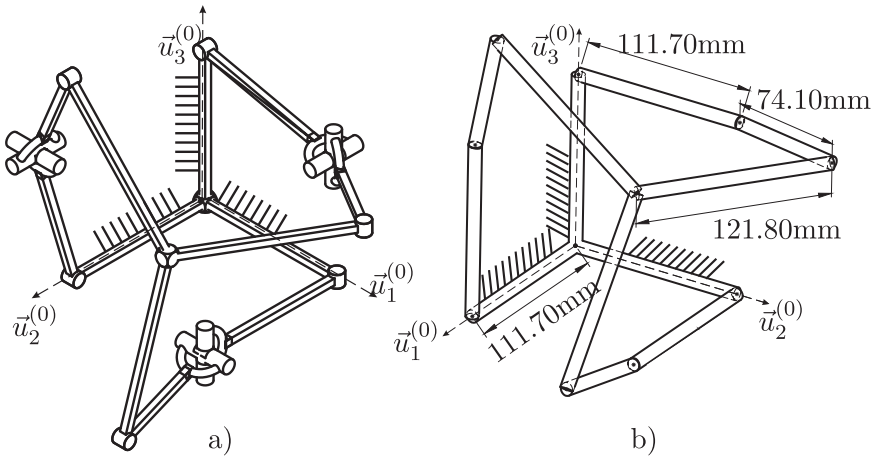

Fig. 11. Sketches of R-CUBE: (a) a CAD model, (b) a simplified CAD model for use in simulations.

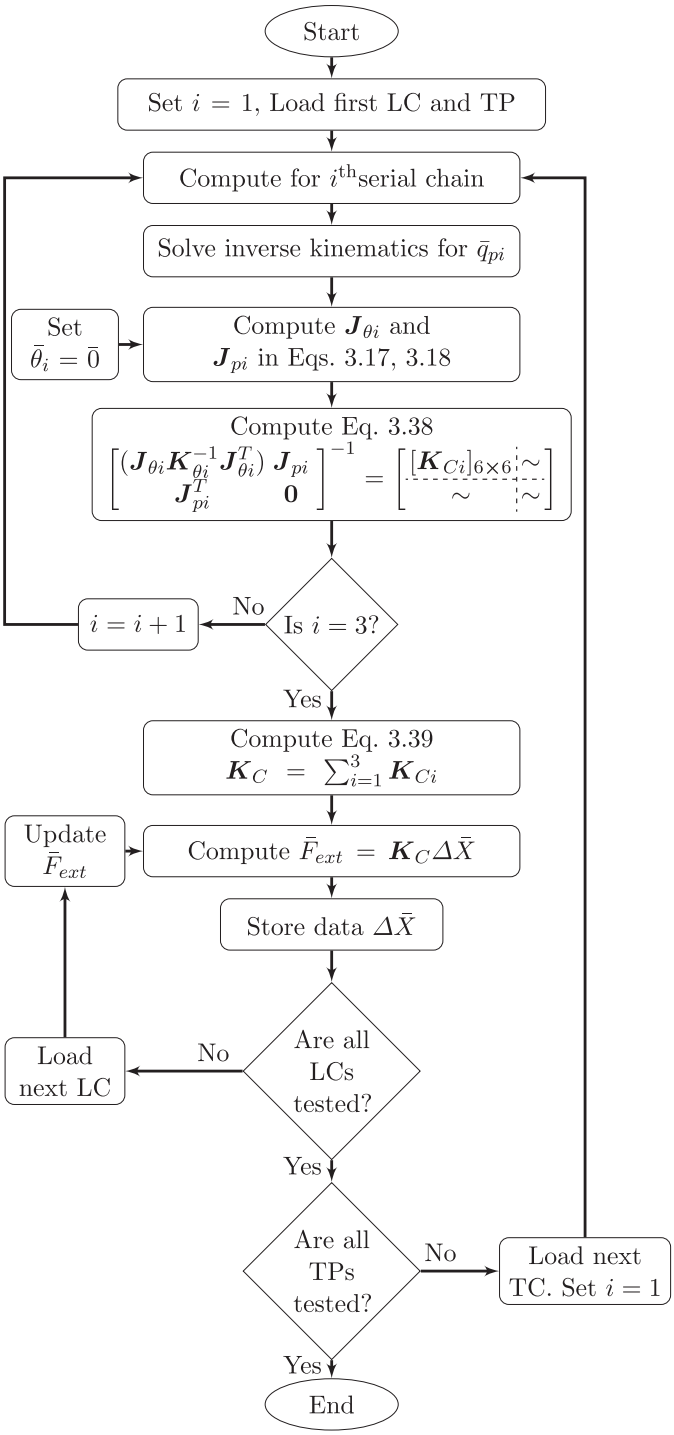

Fig. 12. Flow chart for VJM model simulation.

three remote points of serial chains were connected with each other by using the aforementioned joint options to construct the manipulator structure.

After the abovementioned settings were done, the meshing process was conducted. The mesh size was set to be constant for all links and determined as “4 mm”. This size is the same as the thickness of the tubes. Since the tubes have a regular shape, reducing the mesh size does not affect the accuracy, but it extends the computation time. “Iterative” solver was selected in this FEM analysis to obtain relatively more precise results. If an external wrench is applied to the manipulator,

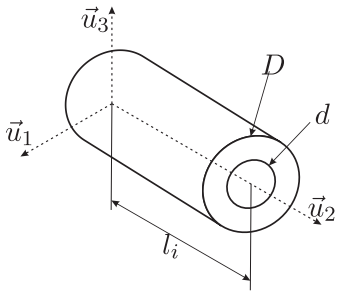

D	10.00mm
d	6.00mm

l_1	111.70mm
l_2	74.10mm
l_3	121.80mm

E	200GPa
G	76.9GPa

Fig. 13. Design variables of *i*th tubular link.

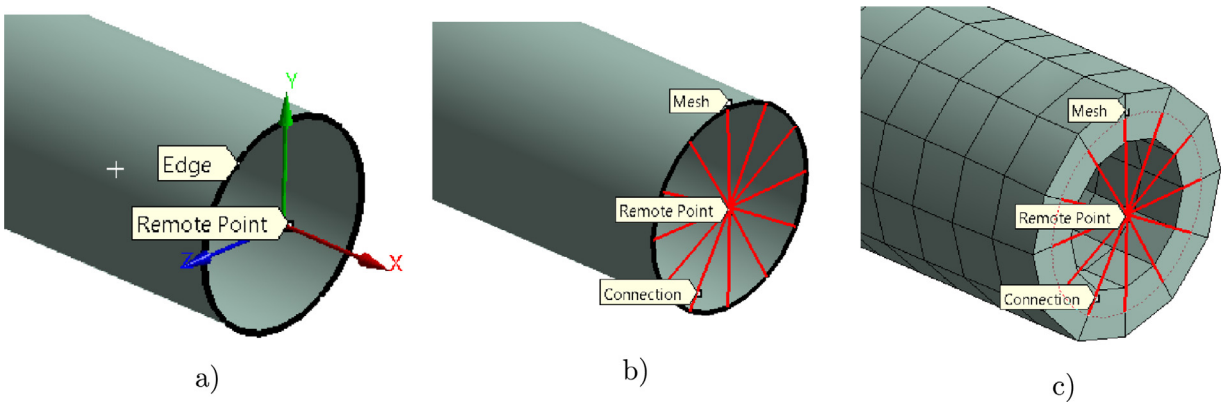

Fig. 14. ANSYS sketches of a link. (a) Reference frame and remote point at the tip of a link, (b) Constraint of the remote point and hollow tube profile, (c) meshed tube structure and remote point.

Fig. 15. Illustration of connections in ANSYS. RP: Remote Point, RJ: Revolute Joint, UJ: Universal Joint, B: Base, MP: Mobile Platform.

force/torque distribution among bodies changes due to compliant deflections. Hence, "Large Deflections" were set to "On" to calculate this change in force/torque distribution. All of the force, torque, displacement, and rotation convergence tolerances were set to 0.05%. Tighter tolerances increase the computation time but do not have an effect on the accuracy of results. A detailed simulation setup information is given in Table 4. A "Parameter Set" was prepared in ANSYS Workbench for 8 LCs. However, 10 TPs were manually set.

5. Results

In this section, FEM and VJM results are presented and compared. First, compliant displacements computed from each model are given. Then, errors between the results obtained from both models are calculated. Finally, the computation times of each model are compared to each other. In addition, a correction term is introduced and applied to VJM model results to increase its accuracy with respect to the FEM results.

5.1. Deflection results of FEM and VJM

A general deflection vector, $\Delta\bar{X}_{hk}$, is given by the following equality:

$$\Delta\bar{X}_{hk} = \left[\Delta\bar{X}^T_{TD,hk} \;\middle|\; \Delta\bar{X}^T_{RD,hk}\right]^T \tag{5.1}$$

TD and *RD* denote the translational and rotational deflections. Subscripts *h* and *k* denote the test point (TP), and load condition (LC), respectively. TDs are examined for force loads, and RDs are investigated for torsional loads. Accordingly, absolute and error percentage between the VJM and the FEM results are computed separately for TD, and RD according to the following equations.

$$\text{Error}_{g,hk} = |\Delta\vec{X}_{VJM,g,hk} - \Delta\vec{X}_{FEM,g,hk}| \tag{5.2}$$

$$\%\text{Error}_{g,hk} = \frac{|\Delta\vec{X}_{VJM,g,hk} - \Delta\vec{X}_{FEM,g,hk}|}{|\Delta\vec{X}_{FEM,g,hk}|} \times 100 \tag{5.3}$$

where subscript *VJM* and *FEM* indicates the simulation type, and *g* denotes TD or RD. Hence, $\Delta\bar{X}_{g,hk}$ has three elements for VJM and FEM.

Absolute translational compliant deflections, $\|\Delta\bar{X}_{TD,hk}\|$, for both FEM and VJM are given in Fig. 16. Relative errors and error percentages are also illustrated in Fig. 16 for all TPs and LCs. Minimum translational compliant deflection values are observed at TP7 in both VJM and FEM results for LC2 and LC7 load conditions. Minimum deflection with VJM is computed as 1.11×10^{-1} mm and minimum deflection with FEM is computed as 1.25×10^{-1} mm. Maximum deflections for VJM and FEM are observed at TP3 for load conditions in between LC2 and LC7. Maximum deflections are computed as 1.18 mm for VJM and 1.3 mm for FEM. Among all LCs and TPs, minimum VJM-FEM error is computed to be 0.014 mm, and the maximum error is obtained as 0.12 mm. In TP7 for LC4 and LC5, error percentage is less than 8% while LC2 and LC7 load conditions' error percentages are up to 12%. In general, error percentages vary between 8% and 10%.

Absolute rotational compliant deflections, $\|\Delta\bar{X}_{RD,hk}\|$, relative errors, and error percentages are given in Fig. 17. The maximum and the minimum VJM rotations are obtained at TP1 and TP9 as 0.4362 and 0.4069 degrees for all LCs. The maximum rotation in FEM is computed at TP1 as 0.5072 degrees for LC2, LC5, and LC8 while the minimum rotation is acquired at TP9 as 0.4393 degrees for LC1, LC4, and LC7. The minimum error is observed as 0.0208 degrees at TP9 for LC4. The maximum error is 0.1008 degrees at TP1 for LC8 and LC5. The minimum error percentage is around 6% while the maximum one is above 12%.

There are two important phenomena for the presented results. The first one is the VJM compliant deflection results are always lower than the FEM results for both translation and rotation. Secondly, rotational deflection results for VJM do not depend on LC change. Both behaviors of VJM model are explained by the linear solution algorithm given in Fig. 12. In order to conduct a direct solution for fast operating algorithm, $\bar{\theta}_i$ is set to $\bar{0}$ to compute $\boldsymbol{J}_{\theta i}$ matrix. Later, this matrix is used for calculating the force/torque distribution of the external wrench on virtual joints. Since $\bar{\theta}_i$ is set to $\bar{0}$, this mapping always considers an undeformed kinematic configuration. FEM, on the other hand, uses an iterative solution process which updates the kinematics in each iteration by issuing the deformations calculated in the previous iteration. Hence, force/torque distribution on FEM nodes are re-computed in each iteration. This iterative computation generates relatively more accurate results. Setting $\bar{\theta}_i$ to $\bar{0}$ also changes the numerical values of $\boldsymbol{C}_C$ matrix elements in Eq. (3.42). When the matrix is computed with $\bar{\theta}_i = \bar{0}$, off-diagonal elements of $\boldsymbol{C}_{CD}$ is equal to 0. Hence, $\boldsymbol{C}_{CD}$ is a diagonal sub-matrix of $\boldsymbol{C}_C$. This indicates that rotational deflections about an axis are generated by the torques that are applied about that specific motion axis. In other words, applying a moment about one axis does not cause rotation about the other axes. This makes the torque/rotation relation decoupled for the investigated manipulator. It should be noted that when an iterative algorithm is employed for VJM, this decoupled behavior will not be observed. Iterative computation causes the generation of non-zero elements in the off-diagonal elements of $\boldsymbol{C}_{CD}$. Nevertheless, FEM updates kinematics after each iteration due to the calculated deformations. Therefore, the LC effect on the rotational deflections becomes visible in FEM simulation.

5.2. Average translational deflection results

Average translational compliant deflections were acquired to evaluate the accuracy of VJM against FEM results. Average translational compliant displacement was computed via the arithmetic mean of the absolute value of compliant displacements at each TP for all LCs. In Fig. 18(a), average translational deflections are illustrated for FEM and VJM results. The

Table 4
ANSYS simulation setup details.

Mesh properties		Analysis settings	
Size Function	Curvature	Solver Target	Mechanical APDL
Relevance Center	Fine	Number of Steps	1
Transition	Slow	Solver Type	Iterative
Span Angle Center	Fine	Weak Springs	On
Curvature Normal Angle	18°	Spring Stiffness	Program Controlled
Min Size	2 mm	Solver Pivot Check	Program Controlled
Max Face Size	4 mm	Large Deflection	On
Max Tet Size	5 mm	Newton–Raphson	Program Controlled
Growth Rate	Default	Force Convergence	On
Remaining Parameters	Default	Moment Convergence	On
Total Nodes	5578	Displacement Convergence	On
Element Type	Quad4 SHELL181	Rotation Convergence	On
		Tolerance	0.05%
		Minimum Reference	0.001 N, 0.001 Nm, 0 m, 0°

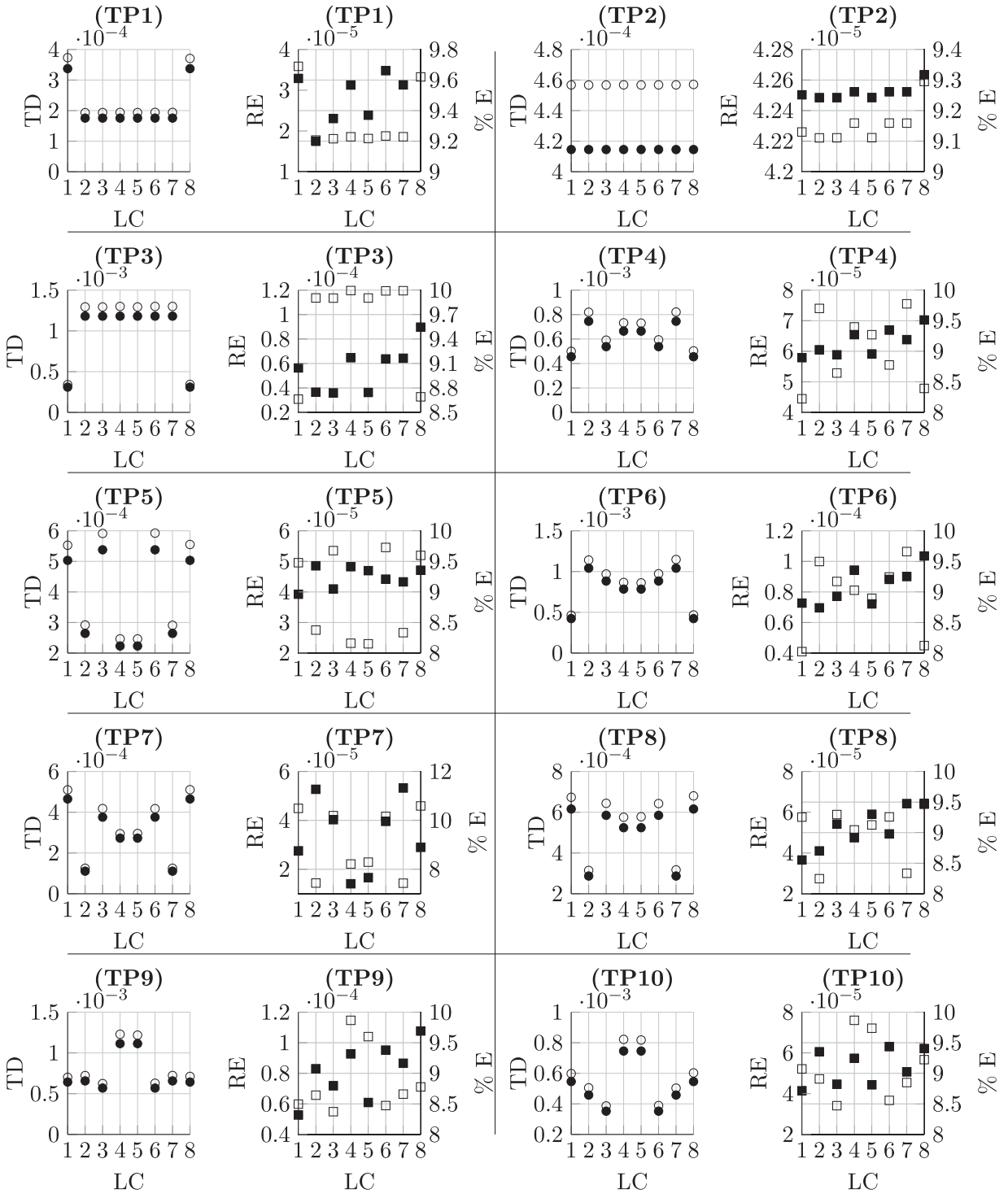

Fig. 16. Translational Deflection (TD) in meters, relative error (RE) in meters, and % errors (%E) are given at each TP with respect to LC. "·" and "∘" denote the results of VJM and FEM, respectively for TD graphs. "■" and "□" denote the % errors and relative errors, respectively for RE - %E graphs.

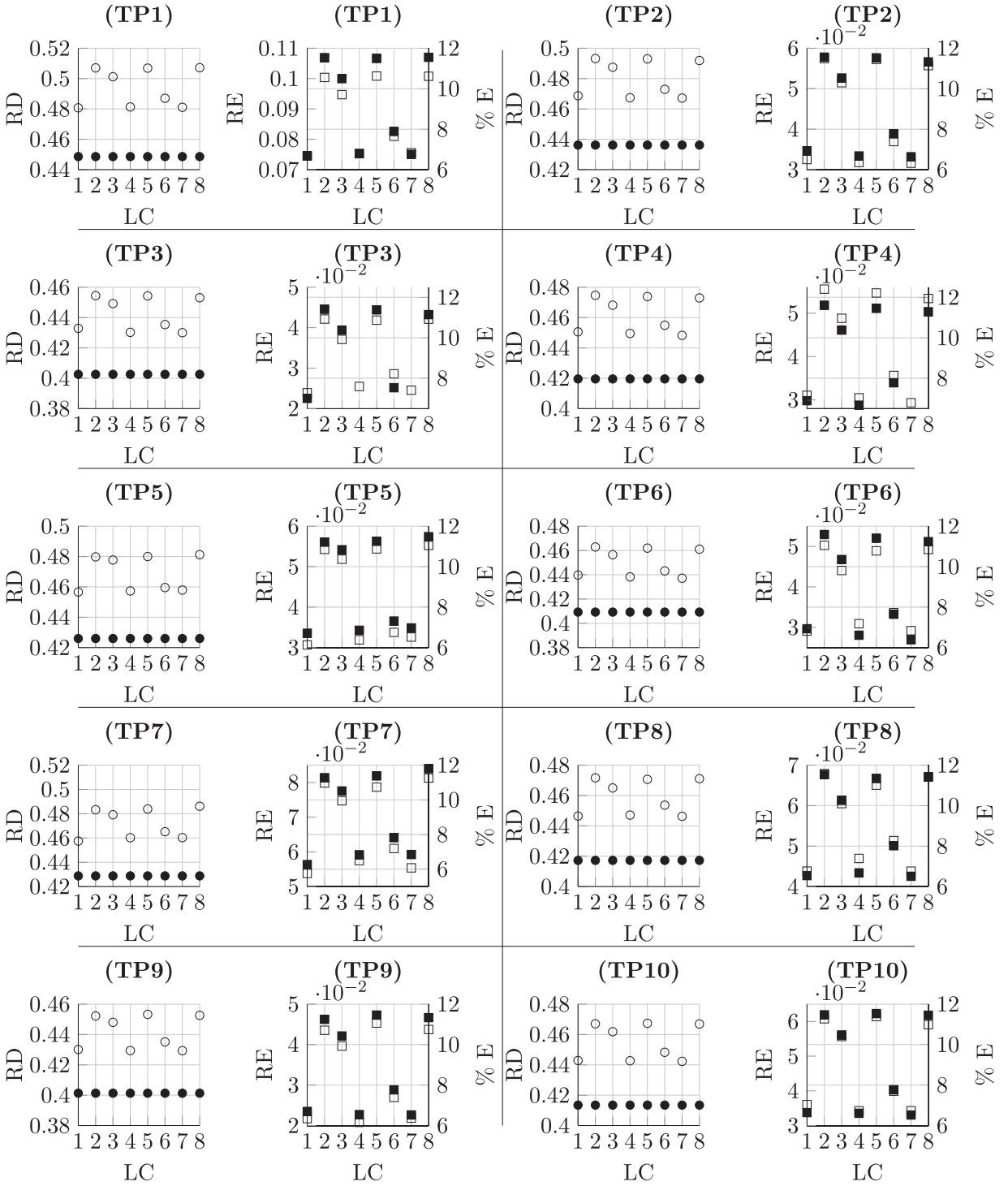

Fig. 17. Rotational Deflection (RD) in degrees, relative error (RE) in degrees, and % errors (%E) are given at each TP with respect to LC. "$\cdot$" and "$\circ$" denote the results of VJM and FEM, respectively for RD graphs. "■" and "□" denote the % errors and relative errors, respectively for RE - %E graphs.

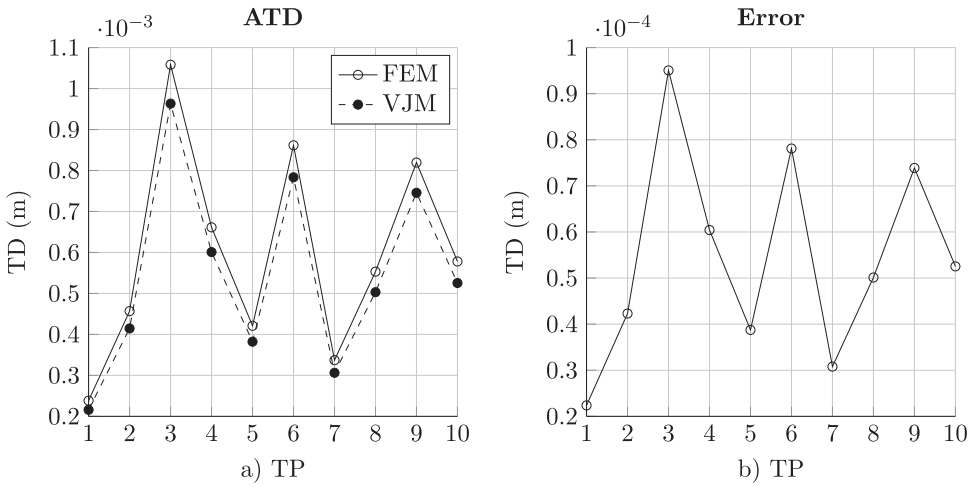

Fig. 18. Compliant deflection and error graphs: (a) Average Translational Deflection (ATD) of VJM and FEM, (b) VJM-FEM ATD error.

deflections obtained in both methods have the same trend in results. At TP3, TP6, and TP9, higher average deflections are observed. In these poses, the relative error of the two methods also increases, as shown in Fig. 18(b). The most and the least stiff poses are TP3 (fully extended pose) and TP1 (fully folded pose), respectively. While the highest errors are obtained at TP3, the lowest errors are observed at TP1. Hence, for more compliant poses of the mechanism, the accuracy of the compliant displacement results obtained from VJM is relatively lower.

In Fig. 19(a)–(c), average compliant deflections calculated with VJM and FEM are given for each motion axis. In these 3 plots, the most and the least compliant deflections are observed at TP3 and TP1, as expected. At TP1, TP2, and TP3, the same amount of deflections are observed along each respective motion axis, since these poses are isotropic poses.

In Fig. 19(d), error percentages of average deflections are illustrated. The error is around 10%. The maximum variation of errors is less than 1% except for $\vec{u}_1^{(0)}$ axis of TP7. The error percentage obtained along $\vec{u}_2^{(0)}$ and $\vec{u}_3^{(0)}$ is relatively smaller than the general error trend. Even though TP1 has the minimum deflection among all results, its error percentage is relatively higher.

Having small compliant deflections makes the error percentage computation more sensitive to numerical errors. For this reason, relatively higher error percentages are calculated for TP1.

TP7 is the second stiffest pose. Hence, smaller compliant deflections are computed at this pose. Similar to TP1, its error percentage is high. However, the error percentage observed at TP7 has a different condition relative to TP1, which is observed by a peak in error percentage. Note that, TP1 is an isotropic pose due to its kinematic configuration. This isotropy makes the VJM and FEM models less nonlinear at this pose. TP7, on the other hand, is not an isotropic pose. As a result of this, the difference between FEM and VJM results is relatively higher in one direction, which is $\vec{u}_1^{(0)}$ axis of TP7.

TP3 is the one in which the lowest error percentage is obtained, even though the highest deflections are computed at the pose. The reason for this is that TP3 is an isotropic pose and the calculated compliant displacements are larger, which decreases the effect of the numerical errors. Finally, we can state that 10% error is obtained by VJM against FEM results with a 1% variation.

Correlation between FEM and VJM results is shown in Fig. 20(a). FEM results are plotted against VJM results. Also, $y(x) = x$ function is plotted. 100% correlation is achieved when the plotted data is on $y(x) = x$ line. In the compliant displacement range between -0.2 mm and 0.2 mm, the results obtained from both models show a high correlation. The corresponding poses to these data have higher stiffness. Accordingly, deflections at these poses are smaller. This makes them closer to the correlation line. Data in between 0.2 mm and 0.8 mm, and -0.8 mm and -0.2 mm show less correlation since the corresponding poses are more compliant. As a result, they are away from the correlation line. It is observed that the plotted data have a linear distribution. Therefore, it is possible to define a line function as $y(x) = mx$ where m denotes the slope. When m is determined, it is possible to compensate for the VJM model errors.

When a line is fitted to data points, its slope is computed as $m = 1.098$. The slope of the perfect correlation line is 1. When it is compared with m, it can be seen that the error is 9.8%, which is the error of VJM as stated earlier. All the results of VJM are multiplied by $m = 1.098$. Next, a corrected correlation graph is plotted, as shown in Fig. 20(b). This time, almost a perfect correlation is achieved. The error percentage is given in Fig. 21.

5.3. Average rotational deflection results

Average rotational compliant deflections were obtained similarly to translational ones, via the arithmetic mean of the absolute value of rotational compliant displacements at each TP for all LCs. In Fig. 22(a), average rotational deflections

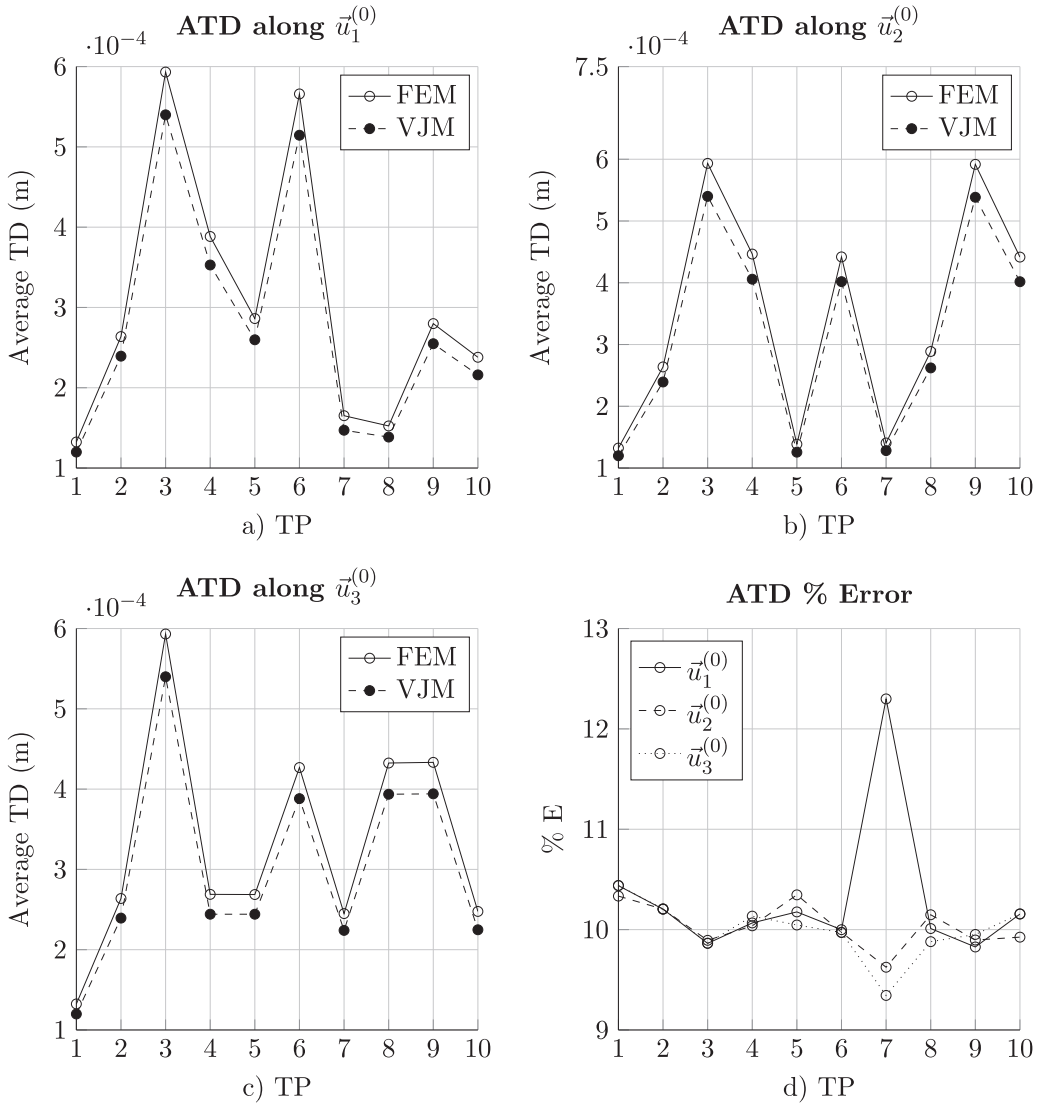

Fig. 19. Compliant deflection and error graphs: (a) ATD along $\vec{u}_1^{(0)}$, (b) ATD along $\vec{u}_2^{(0)}$, (c) ATD along $\vec{u}_3^{(0)}$ and (d) VJM-FEM % error of each axis.

results are given for both, FEM and VJM. Notice that, the rotational deflections in both methods have the same trend. Unlike translational deflections, the highest average deflections are observed at TP1, TP5, and TP7. Similarly, TP3, TP6, and TP9 show high stiffness against the torsional loads. From here, we concluded that the translational and rotational stiffness of R-CUBE mechanism is inversely proportional. Hence, TP1 is the least stiff pose in terms of rotational stiffness while it is the stiffest pose for translational stiffness. Similarly, TP3 has the highest stiffness against torsional loads even though it is the most compliant pose against force loads. The relative error between the methods increases when the deflections are high, as shown in Fig. 22(b). This is the natural result of iterative (FEM) and direct (VJM) solution methods.

In Fig. 23(a)–(c), average compliant deflections are illustrated for each motion axis. TP1, TP2, and TP3 have the same average deflection value for each motion axis since these poses are isotropic. The highest average rotational deflection is observed for $\vec{u}_3^{(0)}$ axis at TP7. The stiffest axis is $\vec{u}_3^{(0)}$ axis at TP9.

In Fig. 23(d), error percentages of average rotational deflections are illustrated. The error is around 10%, and the maximum variation of errors is about 0.2%. Since the relative deflections between the FEM and VJM are large, there is no peak in error percentage graph that is caused by numerical errors.

Rotational deflection correlation is shown in Fig. 24(a). $y(x) = x$ function is plotted as the full correlation line. In the compliant deflections are grouped in the range of $(-0.3^\circ, -0.2^\circ)$, and $(0.2^\circ, 0.3^\circ)$. Since the coupling effect between the axes in terms of rotational stiffness is small, there is no deflection distribution along the correlation line.

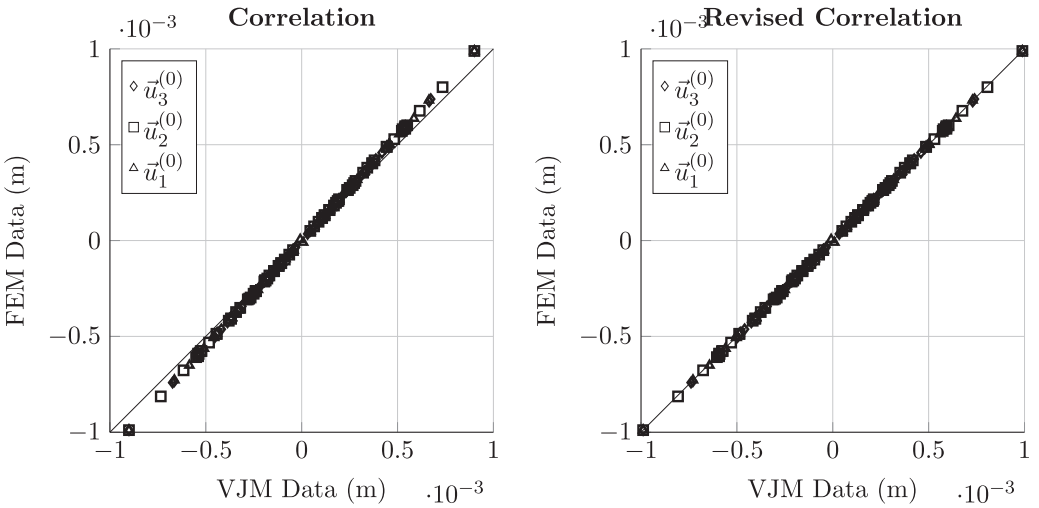

Fig. 20. TD correlations. (a) Correlation with original deflection data. (b) Correlation of FEM with revised VJM data.

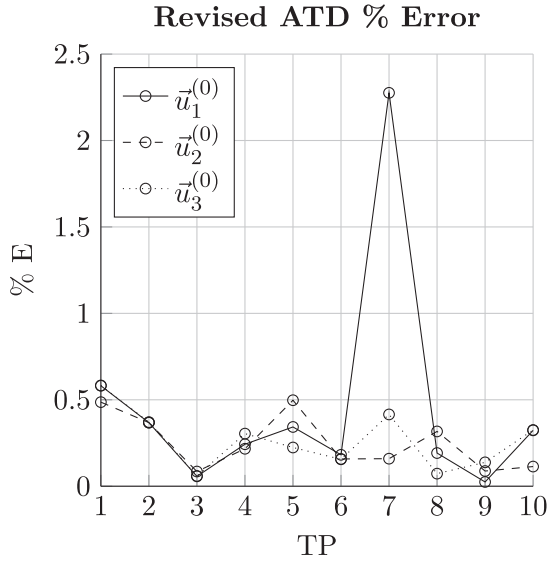

Fig. 21. Revised TD correlations.

The function with the slope of $m = 1.098$ is used for scaling the rotational deflections of VJM results. A corrected correlation graph is plotted, as shown in Fig. 24(b). Again, almost a perfect correlation is achieved. The error percentage is given in Fig. 25, which shows that VJM has an error of less than 0.4%.

5.4. Computation time results

Tests are conducted at 10 TPs and 8 LCs in both ANSYS and MATLAB simulation environments. The simulation tests are carried out on the same computer with the following specifications: 4 Core 2.5 GHz processor and 8GB of RAM. Two cores of the processor are used in ANSYS simulations, while only one core is used in MATLAB simulations. It is observed that computation time does not vary depending on TPs and/or LCs. Computation time is calculated to be 24 s for FEM simulation in ANSYS environment. MATLAB program running the VJM model obtains the solution in 0.0005 s (0.5 ms). Percentage difference in computation time is calculated as follows:

$$\frac{|t_{\text{VJM}} - t_{\text{FEM}}|}{t_{\text{FEM}}} \times 100 = \frac{|0.0005 - 24|}{24} \times 100 = 99.998\% \tag{5.4}$$

where t function shows elapsed time for computation. 99.998% difference is calculated between FEM and VJM calculation durations. Hence, calculations of VJM is significantly faster than FEM.

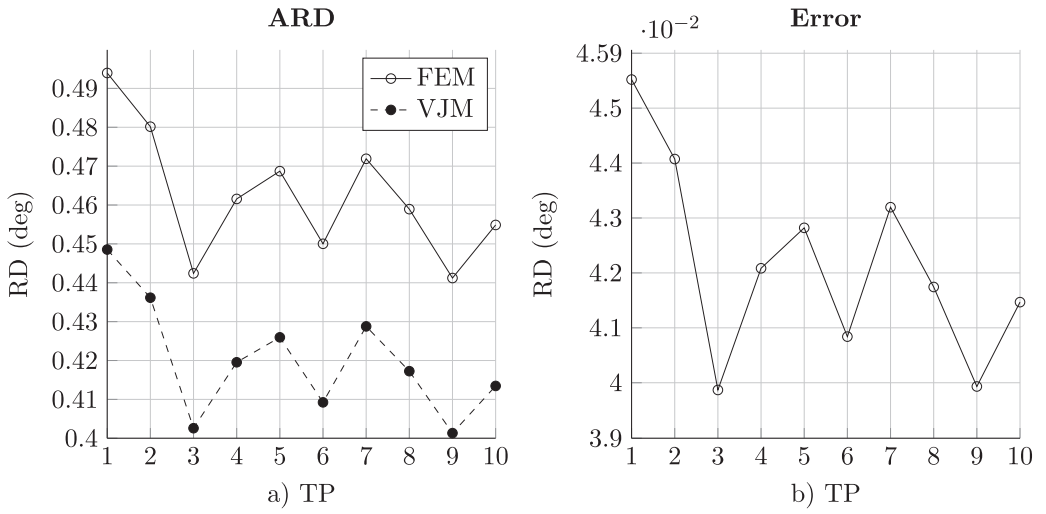

Fig. 22. Compliant deflection and error graphs: (a) Average Rotational Deflection (ARD) of VJM and FEM, (b) VJM-FEM RTD error.

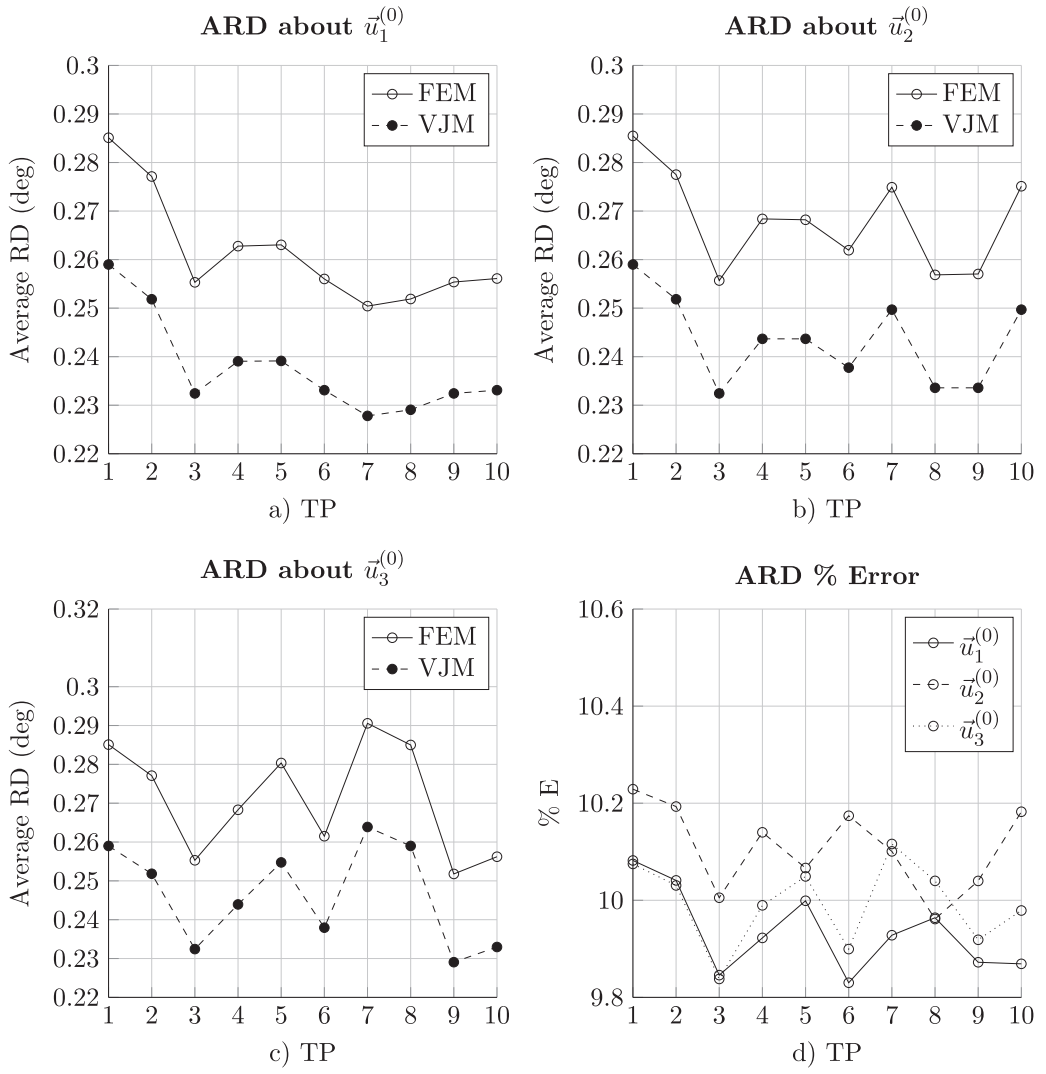

Fig. 23. Compliant deflection and error graphs: (a) ARD about $\vec{u}_1^{(0)}$, (b) ARD about $\vec{u}_2^{(0)}$, (c) ARD about $\vec{u}_3^{(0)}$ and (d) VJM-FEM % error of each axis.

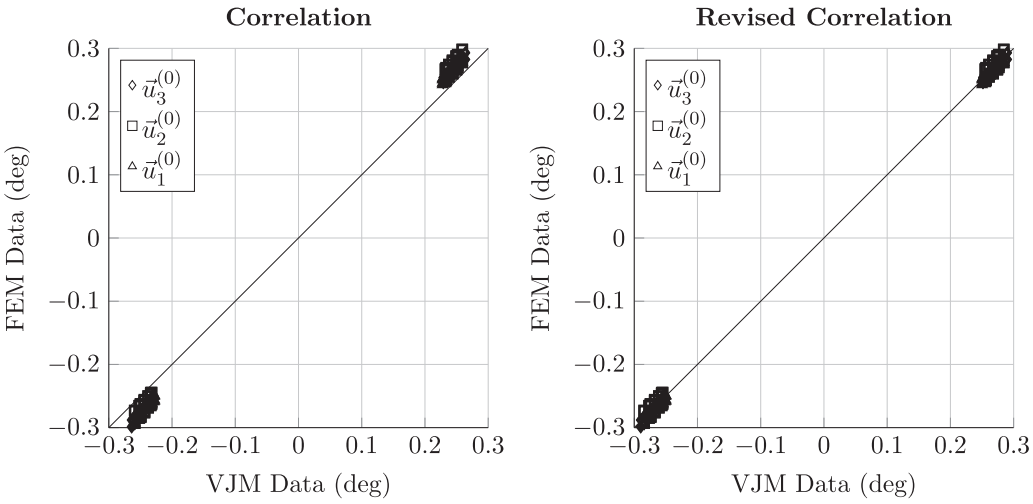

Fig. 24. RD correlations. (a) Correlation with original deflection data. (b) Correlation of FEM with revised VJM data.

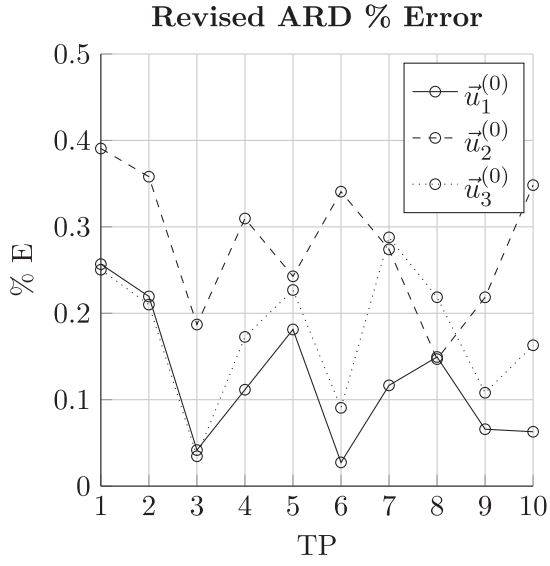

Fig. 25. Revised RD correlations.

6. Conclusion

In this work, a stiffness model of a haptic device's parallel mechanism, R-CUBE mechanism, is investigated to be used in real-time control and optimal design of this haptic device. The main aim is to minimize the computation time while preserving accuracy. Among the other stiffness modeling techniques, VJM is preferred due to its compatibility in a real-time control loop application and also its ability to minimize the duration of a design optimization process.

As a result of the simulation tests, the computation time of VJM is measured to be 0.5 ms, which is 99.998% faster than the FEM solution. Even though VJM is faster, it has about 10% error as compared with FEM results. We have noticed that there is a linear correlation between both models. Hence, a simple scaling constant is used to correct the VJM model. By using the results of FEM, VJM is revised, and the error percentage is reduced to $\sim$1% for translational deflections, and $\sim$0.5% for rotational deflections. Finally, a stiffness model for this specific mechanism and use case is obtained being fast enough for optimal design and real-time-control and being as accurate as the FEM model. However, this correction is only valid for the applied ranges of forces and torques. Therefore, it is necessary to re-evaluate the correction term, which is devised in this article, when a different range of forces/torques is required to be studied. Moreover, a correction term can be obtained as a function of force. If the deflections are small enough, a single scaling factor may be conveniently used for corrections.

As a future study, the VJM model can be calibrated with respect to the experimental results obtained from a prototype, acquired by using experimentally obtained deflection data for correction. In an experimental study, when measuring the

total stiffness of the mechanism, the effect of the stiffness of the joints along with the links are obtained. In this case, when the VJM model is revised with this experimental data, it will include the joint stiffness properties as well since the virtual joints and passive joints are located at the same positions.

Acknowledgements

The first author thanks the ACRI association for a grant which supported him for a period of study at LARM in Cassino/Italy within 2018. The study is supported in part by The Scientific and Technological Research Council of Turkey via grant number 117M405.

The paper presents results from the research activities of the project ID 37_215, MySMIS code 103415 “Innovative approaches regarding the rehabilitation and assistive robotics for healthy ageing” co-financed by the European Regional Development Fund through the Competitiveness Operational Programme 2014–2020, Priority Axis 1, Action 1.1.4, through the financing contract 20/01.09.2016, between the Technical University of Cluj-Napoca and ANCSI as Intermediary Organism in the name and for the Ministry of European Funds.

References

[1] T.A. Kern, Engineering Haptic Devices: A Beginner's Guide for Engineers, Springer Publishing Company, Incorporated, 2009.
[2] M. Vulliez, S. Zeghloul, Multi-objective design optimization of the delthaptic, a new 6-dof haptic device, in: Industrial Informatics (INDIN), 2016 IEEE 14th International Conference on, IEEE, 2016, pp. 248–253.
[3] P. Lambert, J. Herder, A novel parallel haptic device with 7 degrees of freedom, in: World Haptics Conference (WHC), 2015 IEEE, IEEE, 2015, pp. 183–188.
[4] D. Borro, J. Savall, A. Amundarain, J.J. Gil, A. Garcia-Alonso, L. Matey, A large haptic device for aircraft engine maintainability, IEEE Comput. Graph. Appl. 24 (6) (2004) 70–74.
[5] A. Ahmad, K. Andersson, U. Sellgren, A model-based and simulation-driven methodology for design of haptic devices, Mechatronics 24 (7) (2014) 805–818.
[6] C. Zhao, X. Luo, F. Ma, H. Zhang, Transparency design of a new haptic interface, in: Electrical and Control Engineering (ICECE), 2011 International Conference on, IEEE, 2011, pp. 6193–6197.
[7] X.-J. Liu, Z.-L. Jin, F. Gao, Optimum design of 3-dof spherical parallel manipulators with respect to the conditioning and stiffness indices, Mech. Mach. Theory 35 (9) (2000) 1257–1267.
[8] M. Ceccarelli, G. Carbone, E. Ottaviano, Multi criteria optimum design of manipulators, Bull. Polish Acad. Tech. Sci. 53 (2005).
[9] İ. Görgülü, G. Kiper, M.İ.C. Dede, A critical review of unpowered performance metrics of impedance-type haptic devices, in: European Conference on Mechanism Science, Springer, 2018, pp. 129–136.
[10] J.E. Colgate, J.M. Brown, Factors affecting the z-width of a haptic display, in: Robotics and Automation, 1994. Proceedings., 1994 IEEE International Conference on, IEEE, 1994, pp. 3205–3210.
[11] E. Samur, Performance Metrics for Haptic Interfaces, Springer Science & Business Media, 2012.
[12] H. Wang, L. Zhang, G. Chen, S. Huang, Parameter optimization of heavy-load parallel manipulator by introducing stiffness distribution evaluation index, Mech. Mach. Theory 108 (2017) 244–259.
[13] I. Görgülü, M.I.C. Dede, A new stiffness performance index: volumetric isotropy index, MDPI Mach. 7 (2) (2019) 44.
[14] A. Raoofian, A. Taghvaeipour, A. Kamali, On the stiffness analysis of robotic manipulators and calculation of stiffness indices, Mech. Mach. Theory 130 (2018) 382–402.
[15] T. Sun, B. Lian, Stiffness and mass optimization of parallel kinematic machine, Mech. Mach. Theory 120 (2018) 73–88.
[16] E. Esquivel, G. Carbone, M. Ceccarelli, J.C. Jáuregui, A dynamic compensation for roll hemming process, IEEE Access 6 (2018) 18264–18275.
[17] C. Gosselin, Stiffness mapping for parallel manipulators, IEEE Trans. Robot. Autom. 6 (3) (1990) 377–382.
[18] M. Ceccarelli, G. Carbone, A stiffness analysis for Capaman (cassino parallel manipulator), Mech. Mach. Theory 37 (5) (2002) 427–439.
[19] A. Pashkevich, A. Klimchik, D. Chablat, Enhanced stiffness modeling of manipulators with passive joints, Mech. Mach. Theory 46 (5) (2011) 662–679.
[20] W. Li, F. Gao, J. Zhang, R-cube, a decoupled parallel manipulator only with revolute joints, Mech. Mach. Theory 40 (4) (2005) 467–473.
[21] E. Mobedi, İ. Görgülü, M.İ.C. Dede, Experimental evaluation of actuation and sensing capabilities of a haptic device, in: European Conference on Mechanism Science, Springer, 2018, pp. 137–144.
[22] A. Rezaei, A. Akbarzadeh, Influence of joints flexibility on overall stiffness of a 3-prup compliant parallel manipulator, Mech. Mach. Theory 126 (2018) 108–140.
[23] T. Weiser, B. Corves, Deflection modeling of a manipulator for mechanical design, Mech. Mach. Theory 137 (2019) 172–187.
[24] T. Huang, X. Zhao, D.J. Whitehouse, Stiffness estimation of a tripod-based parallel kinematic machine, IEEE Trans. Robot. Autom. 18 (1) (2002) 50–58.
[25] A. Ahmad, K. Andersson, U. Sellgren, S. Khan, A stiffness modeling methodology for simulation-driven design of haptic devices, Eng. Comput. 30 (1) (2014) 125–141.
[26] G. Dhatt, E. Lefran, G. Touzot, Finite Element Method, John Wiley & Sons, 2012.
[27] G. Piras, W. Cleghorn, J. Mills, Dynamic finite-element analysis of a planar high-speed, high-precision parallel manipulator with flexible links, Mech. Mach. Theory 40 (7) (2005) 849–862.
[28] A. Pashkevich, D. Chablat, P. Wenger, Stiffness analysis of overconstrained parallel manipulators, Mech. Mach. Theory 44 (5) (2009) 966–982.
[29] Z. Gao, D. Zhang, Simulation driven performance characterization of a spatial compliant parallel mechanism, Int. J. Mech. Mater.Des. 10 (3) (2014) 227–246.
[30] W.-a. Cao, H. Ding, A method for stiffness modeling of 3r2t overconstrained parallel robotic mechanisms based on screw theory and strain energy, Precis. Eng. 51 (2018) 10–29.
[31] W.-a. Cao, D. Yang, H. Ding, A method for stiffness analysis of overconstrained parallel robotic mechanisms with scara motion, Robot. Comput. Integrated Manuf. 49 (2018) 426–435.
[32] H.C. Martin, Introduction to Matrix Methods of Structural Analysis, McGraw-Hill, 1966.
[33] A. Ghali, A. Neville, T.G. Brown, Structural Analysis: A Unified Classical and Matrix Approach, CRC Press, 2014.
[34] Y.-W. Li, J.-S. Wang, L.-P. Wang, Stiffness analysis of a Stewart platform-based parallel kinematic machine, in: Robotics and Automation, 2002. Proceedings. ICRA'02. IEEE International Conference on, vol. 4, IEEE, 2002, pp. 3672–3677.
[35] D. Deblaise, X. Hernot, P. Maurine, A systematic analytical method for PKM stiffness matrix calculation, in: Robotics and Automation, 2006. ICRA 2006. Proceedings 2006 IEEE International Conference on, IEEE, 2006, pp. 4213–4219.
[36] S. Shi, H. Wu, Y. Song, H. Handroos, M. Li, Y. Cheng, B. Mao, Static stiffness modelling of east articulated maintenance arm using matrix structural analysis method, Fusion Eng. Des. 124 (2017) 507–511.
[37] A. Klimchik, A. Pashkevich, Stiffness modelling of serial under-constrained manipulators using matrix structural analysis, IFAC-PapersOnLine 51 (11) (2018) 710–715.

[38] A. Klimchik, D. Chablat, A. Pashkevich, Stiffness modeling for perfect and non-perfect parallel manipulators under internal and external loadings, Mech. Mach. Theory 79 (2014) 1–28.
[39] A. Klimchik, A. Pashkevich, D. Chablat, Fundamentals of manipulator stiffness modeling using matrix structural analysis, Mech. Mach. Theory 133 (2019) 365–394.
[40] T. Sun, B. Lian, Y. Song, Stiffness analysis of a 2-dof over-constrained RPM with an articulated traveling platform, Mech. Mach. Theory 96 (2016) 165–178.
[41] B. Lian, T. Sun, Y. Song, Y. Jin, M. Price, Stiffness analysis and experiment of a novel 5-dof parallel kinematic machine considering gravitational effects, Int. J. Mach. Tools Manuf. 95 (2015) 82–96.
[42] H. Liu, T. Huang, D.G. Chetwynd, A. Kecskemthy, Stiffness modeling of parallel mechanisms at limb and joint/link levels, IEEE Trans. Robot. 33 (3) (2017) 734–741, doi:10.1109/TRO.2017.2654499.
[43] B. Taner, M.I.C. Dede, Image processing based stiffness mapping of a haptic device, in: New Advances in Mechanisms, Mechanical Transmissions and Robotics, Springer, 2017, pp. 447–454.
[44] J.K. Salisbury, J.J. Craig, Articulated hands: force control and kinematic issues, Int. J. Robot. Res. 1 (1) (1982) 4–17.
[45] C. Gosselin, Stiffness analysis of parallel mechanisms using a lumped model, Int. J. Robot. Autom. 17 (2002) 17–27.
[46] G. Wu, S. Bai, J. Kepler, Mobile platform center shift in spherical parallel manipulators with flexible limbs, Mech. Mach. Theory 75 (2014) 12–26.
[47] A.G. Hoevenaars, P. Lambert, J.L. Herder, Jacobian-based stiffness analysis method for parallel manipulators with non-redundant legs, Proc. Inst. Mech. Eng. Part C 230 (3) (2016) 341–352.
[48] G. Carbone, Stiffness analysis and experimental validation of robotic systems, Front. Mech. Eng. 6 (2) (2011) 182–196.
[49] X. Gao, S.-M. Song, C.Q. Zheng, A generalized stiffness matrix method for force distribution of robotic systems with indeterminancy, ASME J. Mech. Des. 115 (3) (1993) 585–591.
[50] W.-a. Cao, H. Ding, W. Zhu, Stiffness modeling of overconstrained parallel mechanisms under considering gravity and external payloads, Mech. Mach. Theory 135 (2019) 1–16.
[51] C. Yang, Q. Li, Q. Chen, L. Xu, Elastostatic stiffness modeling of overconstrained parallel manipulators, Mech. Mach. Theory 122 (2018) 58–74.
[52] C. Quennouelle, C. Gosselin, Stiffness matrix of compliant parallel mehanisms, in: ASME 2008 International Design Engineering Technical Conferences and Computers and Information in Engineering Conference, American Society of Mechanical Engineers, 2008, pp. 151–161.
[53] A. Rezaei, A. Akbarzadeh, M.-R. Akbarzadeh-T, An investigation on stiffness of a 3-psp spatial parallel mechanism with flexible moving platform using invariant form, Mech. Mach. Theory 51 (2012) 195–216.
[54] S. Yan, S. Ong, A. Nee, Stiffness analysis of parallelogram-type parallel manipulators using a strain energy method, Robot. Comput. Integrated Manuf. 37 (2016) 13–22.
[55] I. Görgülü, Optimal Design of a Kinesthetic Haptic Device Mechanism for Enhancing its Impedance Characteristics, Thesis (Master). Izmir Institute of Technology, Mechanical Engineering, 2018.